**WILEY**

# Modeling isovolumetric phases in cardiac flows by an Augmented Resistive Immersed Implicit Surface method

**Alberto Zingaro**[1,2] ⬤  |  **Michele Bucelli**[1] ⬤  |  **Ivan Fumagalli**[1] ⬤  |
**Luca Dede'**[1] ⬤  |  **Alfio Quarteroni**[1,3]

[1]MOX, Laboratory of Modeling and Scientific Computing, Dipartimento di Matematica, Politecnico di Milano, Milan, Italy

[2]ELEM Biotech S.L., Barcelona, Spain

[3]Institute of Mathematics, École Polytechnique Fédérale de Lausanne, Lausanne, Switzerland

**Correspondence**
Michele Bucelli, MOX, Laboratory of Modeling and Scientific Computing, Dipartimento di Matematica, Politecnico di Milano, Piazza Leonardo da Vinci, 32, 20133 Milan, Italy.
Email: michele.bucelli@polimi.it

**Abstract**
A major challenge in the computational fluid dynamics modeling of the heart function is the simulation of isovolumetric phases when the hemodynamics problem is driven by a prescribed boundary displacement. During such phases, both atrioventricular and semilunar valves are closed: consequently, the ventricular pressure may not be uniquely defined, and spurious oscillations may arise in numerical simulations. These oscillations can strongly affect valve dynamics models driven by the blood flow, making unlikely to recovering physiological dynamics. Hence, prescribed opening and closing times are usually employed, or the isovolumetric phases are neglected altogether. In this article, we propose a suitable modification of the Resistive Immersed Implicit Surface (RIIS) method (Fedele et al., Biomech Model Mechanobiol 2017, 16, 1779–1803) by introducing a reaction term to correctly capture the pressure transients during isovolumetric phases. The method, that we call Augmented RIIS (ARIIS) method, extends the previously proposed ARIS method (This et al., Int J Numer Methods Biomed Eng 2020, 36, e3223) to the case of a mesh which is not body-fitted to the valves. We test the proposed method on two different benchmark problems, including a new simplified problem that retains all the characteristics of a heart cycle. We apply the ARIIS method to a fluid dynamics simulation of a realistic left heart geometry, and we show that ARIIS allows to correctly simulate isovolumetric phases, differently from standard RIIS method. Finally, we demonstrate that by the new method the cardiac valves can open and close without prescribing any opening/closing times.

**KEYWORDS**
cardiac hemodynamics, cardiac modeling, valves

Alberto Zingaro and Michele Bucelli equally contributed to this work.

# 1 | INTRODUCTION

During the heart cycle, there are two phases in which all cardiac valves are closed and the action of the ventricular displacement affects blood pressure without a net flow. In the left ventricle (the same applies for the right part of the heart), during the *isovolumetric contraction*, the intraventricular pressure raises up to the point in which the aortic valve opens for the systolic ejection, while in the *isovolumetric relaxation* the ventricular pressure decreases until reaching the atrial one, thus leading to the opening of the mitral valve.[1,2] Cardiac valve dynamics is mainly driven by transvalvular pressure drop.[3] Hence, an accurate modeling of the isovolumetric phases in which the intraventricular pressure undergoes rapid changes is an essential prerequisite to capture valve opening and closing, and to properly model their effect on the flow.

The behavior of blood pressure in the heart chambers is determined by the contraction and relaxation of the myocardium. With this in mind, Fluid–Structure Interaction (FSI) models coupling the blood flow with the heart mechanics have been proposed in the literature,[4–9] or even more realistic electrophysiology-mechanics-hemodynamics models as in, for example, References [10–14]. However, these coupled models typically entail a high computational cost, and they require a challenging calibration of a huge number of physical parameters, especially in pathological conditions. Because of this, uncoupled (or one-way coupled) approaches have been proposed, to address the sole Computational Fluid Dynamics (CFD) component of the system, with the ventricular displacement prescribed as data coming from analytical functions,[15–20] clinical measurements,[21–27] or from electromechanical simulations.[28–33] Such models mainly differ in the treatment of the valve geometry and dynamics. Mesh-conforming approaches are based on a classical Arbitrary Lagrangian–Eulerian formulation of the flow equations,[34–38] and they include the Resistive Immersed Surface (RIS) method.[39,40] These methods sharply track the valve surfaces, but they entail possible issues regarding large mesh deformations and topological changes at valve closure.[41] To avoid the need of a complete remeshing of the computational domain, while maintaining a sharp description of the valve surface, different XFEM/cutFEM methods have been proposed,[42–48] but their use to simulate cardiac flows at the organ scale has been limited by their relatively high computational cost. On the other hand, fully Eulerian approaches, such as the immersed boundary method,[49–57] the fictitious domain method[58–64] or the Resistive Immersed Implicit Surface (RIIS) method,[21,65] hinge upon an implicit representation of the leaflets and do not require mesh conformity between the fluid domain and the valves. This allows to track the fluid-valve interface, possibly moving in time, without requiring the fluid mesh to follow the valve. For further details and comparisons among different valve models, we refer the reader to References [66–68].

In most of the abovementioned simulations, however, the isovolumetric phases of the heartbeat are neglected due to the non-unique definition of pressure in the ventricle when all valves are closed.[29,30,69–71] This shortcoming is related to the absence of a stress condition on the fluid domain, that would otherwise ensure a correct description of the pressure during isovolumetric phases. This is observed for instance in References [5,8–10,13], where fully-coupled FSI models are used. Modeling accurately these phases is crucial to simulate the entire cardiac cycle, but also for opening and closing cardiac valves in a way that is driven by the blood flow. Indeed, if the pressure is not correctly simulated in these phases, but is instead subject to large and spurious oscillations, it cannot be used as a driver to open and close cardiac valves.

Some studies have circumvented this issue by introducing a slight compressibility of blood—see, for example, References [9,72,73]. However, this assumption may affect the simulation results also in the ejection and filling phases, and the assumption of blood incompressibility is quite established in the cardiovascular modeling community.[71,74–76] A way to overcome pressure non-determination, while preserving incompressibility, is provided by the Augmented Resistive Immersed Surface (ARIS) proposed in Reference [29]: when both the mitral and the aortic valves are closed, the RIS method is augmented with a source term concentrated on the valves, to impose a prescribed value for the pressure.

In this work, we introduce an *Augmented Resistive Immersed Implicit Surface* (ARIIS) method that extends the ARIS capability of treating isovolumetric phases to the framework of the RIIS method, thus supporting valves whose mesh is independent of the background fluid mesh and that can move independently of it (cf. Table 1). To quantitatively assess

**TABLE 1** Features characterizing the RIS, RIIS, ARIS, and ARIIS methods.

|  | Conforming mesh | Non-conforming mesh |
| --- | --- | --- |
| No isovolumetric phases | RIS[40] | RIIS[65] |
| Isovolumetric phases | ARIS[29] | ARIIS |

the results of the method, we propose a simulation setting in a simplified geometry that retains all the characteristics of the heart cycle and may be employed as a benchmark for cardiac hemodynamic solvers. Moreover, we discuss the application of our method to a realistic geometry of the left heart, with a prescribed displacement coming from electromechanical simulations.

The structure of the article is the following. In Section 2, we recall the RIIS method and derive the ARIIS method to prescribe the intraventricular pressure. Then, in Section 3, we assess our new method in different scenarios: first, in Section 3.1, we analyze the idealized case discussed in Reference 29; then, in Section 3.2, we propose a simplified benchmark setting entailing ventricular contraction; a cardiac case in a realistic geometry is considered in Section 3.3. Finally, in Section 3.4, we show that the novel method allows to open and close the valves according to the blood flow conditions, without prescribing opening and closing times a priori.

## 2 | MATHEMATICAL MODEL

In this section, we describe the cardiac hemodynamic model and we introduce a new augmented version of the RIIS method. Specifically, Section 2.1 is devoted to the Navier–Stokes equations in ALE framework with RIIS modeling of valves, and Section 2.2 to the derivation of the ARIIS method.

### 2.1 | The RIIS method for Navier–Stokes equations in ALE form

In heart chambers, blood can be considered as an incompressible, viscous, and Newtonian fluid.[1] Let $\mathbf{u} : \Omega \times (0, T) \to \mathbb{R}^3$ and $p : \Omega \times (0, T) \to \mathbb{R}$ be the fluid velocity and pressure, respectively, where $T$ is the final computational time, and $\Omega$ the domain in current configuration at time $t$, with $t \in (0, T)$. The domain at any time $t$ is defined in terms of a displacement field $\mathbf{d} : \Omega_0 \times (0, T) \to \mathbb{R}^3$ as follows:

$$\Omega = \left\{ \mathbf{x} \in \mathbb{R}^3 : \mathbf{x} = \mathbf{x}_0 + \mathbf{d}(\mathbf{x}_0, t), \mathbf{x}_0 \in \Omega_0 \right\}.$$

Notice that $\Omega$ is a time-dependent domain, but we omit the subscript $t$ to keep the notation simpler, and $\Omega_0$ is the domain in its reference configuration. Furthermore, we denote by $\mathbf{u}_{\mathrm{ALE}} : \Omega \times (0, T) \to \mathbb{R}^3$ the ALE velocity[77,78] and we compute it by deriving $\mathbf{d}$ with respect to time. The domain displacement is the solution of the following harmonic extension problem:

$$\begin{cases} -\nabla \cdot (\psi \nabla \mathbf{d}) = 0 & \text{in } \Omega_0 \times (0, T), \quad \text{(a)} \\ \mathbf{d} = \mathbf{d}_{\partial\Omega}(\mathbf{x}, t) & \text{on } \partial\Omega_0 \times (0, T), \quad \text{(b)} \end{cases} \tag{1}$$

where $\mathbf{d}_{\partial\Omega} : \partial\Omega_0 \times (0, T) \to \mathbb{R}^3$ is the boundary displacement (which is prescribed), and $\psi(\mathbf{x}, t) : \Omega_0 \times (0, T) \to \mathbb{R}$ is a spatially varying stiffening factor used to avoid mesh element distortion. The definition of $\psi$ is given in Section 3 depending on the test cases considered.

To model the cardiac valves with the RIIS method, we consider a time-dependent surface $\Gamma_k(t)$ immersed in $\Omega$, with $k \in \mathcal{I}_v$ (the set of immersed surfaces). We impose kinematic coupling between the surface and the fluid by penalizing the mismatch between the relative fluid velocity $\mathbf{u} - \mathbf{u}_{\mathrm{ALE}}$ and the velocity of the immersed surface $\mathbf{u}_{\Gamma_k}$, that is, by adding to the Navier–Stokes momentum equation the term

$$\frac{R_k}{\varepsilon_k} \delta_k(\varphi_k)(\mathbf{u} - \mathbf{u}_{\mathrm{ALE}} - \mathbf{u}_{\Gamma_k}). \tag{2}$$

For each surface, $\varphi_k : \Omega \times (0, T) \to \mathbb{R}$ denotes its signed distance function, such that, for all $k \in \mathcal{I}_v$, $|\varphi_k(\mathbf{x}, t)| = \mathrm{dist}(\mathbf{x}, \Gamma_k(t))$ and $\Gamma_k(t) = \{\mathbf{x} \in \Omega : \varphi_k(\mathbf{x}, t) = 0\}$. $\Gamma_k$ is characterized by a resistance coefficient $R_k$ and a parameter $\varepsilon_k$ representing the half-thickness of the valve. The penalization is imposed in a narrow layer around $\Gamma_k$, represented by the smoothed Dirac delta function $\delta_k$, defined as

$$\delta_k(\varphi_k) = \begin{cases} \dfrac{1 + \cos(\pi\varphi_k/\varepsilon_k)}{2\varepsilon_k} & \text{if } |\varphi_k| \leq \varepsilon_k, \\ 0 & \text{if } |\varphi_k| > \varepsilon_k, \end{cases}$$

with $\mathbf{x} \in \Omega$ and for all $k \in \mathcal{I}_v$. If the ratio $R_k/\varepsilon_k$ is sufficiently large, the term (2) weakly imposes the condition $\mathbf{u} - \mathbf{u}_{\mathrm{ALE}} = \mathbf{u}_{\Gamma_k}$ over $\Gamma_k$.

The immersed surfaces $\Gamma_k$ can move over time. Let us denote by $\Gamma_k^0$ a fixed reference configuration. The time-dependent displacement of the immersed surface is obtained by summing the ALE displacement $\mathbf{d}$ to a known displacement field $\mathbf{d}_k : \Gamma_k^0 \times (0, T) \to \mathbb{R}^3$ that describes the surface's change of configuration (e.g., from the closed to the open state for cardiac valves). We assume that $\mathbf{d}_k(\mathbf{x}, t) = c_k(t)\widetilde{\mathbf{d}}_k(\mathbf{x})$, and assume that $\widetilde{\mathbf{d}}_k$ is known, while the opening coefficient $c_k(t)$ can be either prescribed or computed according to a suitable model[79] or flow-based rule.[30] The time-dependent configuration of the immersed surface is given by

$$\Gamma_k(t) = \left\{ \mathbf{x} = \mathbf{x}_0 + \mathbf{d}(\mathbf{x}_0) + \mathbf{d}_k(\mathbf{x}_0, t), \ \mathbf{x}_0 \in \Gamma_k^0 \right\}. \tag{3}$$

In some situations, it may be useful to have the surface appear and disappear to simulate the closing and opening of a valve. In that setting, the coefficient $c_k$ varies instantaneously between 0 (closed configuration) and 1 (open configuration), and the resistive term is turned off when $c_k = 1$. This is the strategy followed in the tests of Sections 3.1 and 3.2. For additional details on the RIIS method, we refer the reader to References 21,65.

The incompressible Navier–Stokes equations in the ALE framework with RIIS modeling of cardiac valves read as follows[21]:

$$\begin{cases} \rho\left(\dfrac{\partial \mathbf{u}}{\partial t} + ((\mathbf{u} - \mathbf{u}_{\mathrm{ALE}}) \cdot \nabla)\mathbf{u}\right) - \nabla \cdot (\mu(\nabla\mathbf{u} + \nabla^T\mathbf{u})) + \nabla p + \displaystyle\sum_{k \in \mathcal{I}_v} \dfrac{R_k}{\varepsilon_k} \delta_k(\varphi_k)(\mathbf{u} - \mathbf{u}_{\mathrm{ALE}} - \mathbf{u}_{\Gamma_k}) = \mathbf{0} & \text{in } \Omega \times (0, T) & \text{(a)} \\ \nabla \cdot \mathbf{u} = 0 & \text{in } \Omega \times (0, T) & \text{(b)} \\ \mathbf{u} = \mathbf{g} & \text{on } \Gamma_D \times (0, T) & \text{(c)} \\ \mu(\nabla\mathbf{u} + \nabla^T\mathbf{u})\mathbf{n} - p\mathbf{n} = \mathbf{h} & \text{on } \Gamma_N \times (0, T) & \text{(d)} \\ \mathbf{u} = \mathbf{u}_0 & \text{in } \Omega \times \{0\} & \text{(e)}, \end{cases} \tag{4}$$

where, $\Gamma_D$ and $\Gamma_N$ are Dirichlet and Neumann boundaries, respectively, and $\mathbf{g}$, $\mathbf{h}$ and $\mathbf{u}_0$ are suitable initial and boundary data. We denote the different terms appearing in (4a) as follows:

- inertial term: $\mathcal{I}(\mathbf{u}) = \rho\left(\frac{\partial \mathbf{u}}{\partial t} + ((\mathbf{u} - \mathbf{u}_{\mathrm{ALE}}) \cdot \nabla)\mathbf{u}\right)$;
- viscous term: $\mathcal{D}(\mathbf{u}) = \nabla \cdot \left(\mu(\nabla\mathbf{u} + \nabla^T\mathbf{u})\right)$;
- resistive term: $\mathcal{R}(\mathbf{u}) = \sum_{k \in \mathcal{I}_v} \frac{R_k}{\varepsilon_k} \delta_k(\varphi_k)(\mathbf{u} - \mathbf{u}_{\mathrm{ALE}} - \mathbf{u}_{\Gamma_k})$.

Let us introduce the following function spaces:

$$V = \left\{ \mathbf{v} \in \left[H^1(\Omega)\right]^3 : \mathbf{v} = \mathbf{g} \text{ on } \Gamma_D \right\},$$

$$V_0 = \left\{ \mathbf{v} \in \left[H^1(\Omega)\right]^3 : \mathbf{v} = \mathbf{0} \text{ on } \Gamma_D \right\},$$

$$Q = L^2(\Omega).$$

Then, the weak formulation associated to the problem, derived with standard techniques,[80] reads: find $\mathbf{u}(t) \in V$ and $p \in Q$ such that $\mathbf{u}(0) = \mathbf{u}_0$ and, for all $\mathbf{v} \in V_0$ and $q \in Q$, there holds

$$\left(\rho\left(\frac{\partial \mathbf{u}}{\partial t}+((\mathbf{u}-\mathbf{u}_{\text{ALE}})\cdot\boldsymbol{\nabla})\mathbf{u}\right),\mathbf{v}\right)+\left(\mu(\boldsymbol{\nabla}\mathbf{u}+\boldsymbol{\nabla}^T\mathbf{u}),\boldsymbol{\nabla}\mathbf{v}\right)-(p,\boldsymbol{\nabla}\cdot\mathbf{v})$$
$$+\sum_{k\in\mathcal{I}_v}\left(\frac{R_k}{\varepsilon_k}\delta_k(\varphi_k)(\mathbf{u}-\mathbf{u}_{\text{ALE}}-\mathbf{u}_{\Gamma_k}),\mathbf{v}\right)+(q,\boldsymbol{\nabla}\cdot\mathbf{u})=(\mathbf{h},\mathbf{v})_{\Gamma_N},$$

where $(\cdot,\cdot)$ denotes the $L^2(\Omega)$ inner product, and $(\cdot,\cdot)_{\Gamma_N}$ denotes the $L^2(\Gamma_N)$ inner product.

### 2.1.1 | Numerical discretization

We rely on the finite element method for the spatial discretization of the model equations (1) and (4). The domain $\Omega$ is discretized using a tetrahedral mesh, and the immersed surfaces $\Gamma_k$ are discretized using a triangular mesh. We use piecewise linear finite elements for all variables ($\mathbf{d}$, $\mathbf{u}$ and $p$). Navier–Stokes equations are endowed with either SUPG-PSPG[81] or VMS-LES[16,82,83] stabilization, to allow using equal order elements for velocity and pressure (see Section 3).

We discretize in time using finite differences of the first order. Let $\Delta t$ be the temporal discretization step, $t^n = n\Delta t$ be the discrete times, and let us denote with the superscript $n$ the approximation of time-dependent quantities at time $t^n$ (e.g., $\mathbf{u}^n \approx \mathbf{u}(t^n)$). The domain displacement, surface displacement and fluid equations are solved in a segregated way, as described by Algorithm 1. The non-linearity induced by the advection term in (4a) is treated in a semi-implicit way.[80]

We remark that, at any discrete time $t^n$, the immersed surface $\Gamma_k^n$ is computed by suitably displacing the nodes of the associated mesh, and the signed distance function $\varphi_k^n$ is subsequently recomputed. This is different from the strategy adopted in References 21,65, where the signed distance function for a given valve configuration is obtained by suitably interpolating the distance functions associated to the open and closed valve configurations. Moreover, we point out that the surfaces can move independently of the background fluid mesh, since the two discretizations are not required to be conforming. However, for the smoothed Dirac delta function to be represented correctly, and thus for the method to be effective in imposing the kinematic condition, a sufficient number of fluid mesh elements should lie within distance $\epsilon$ of the immersed surface. As empirically shown in Reference 65, a sufficient condition for this to hold is that $\varepsilon \geq 1.5h$, where $h$ is the mesh size in the vicinity of the surface.

## 2.2 | The ARIIS method

In this section, we derive the ARIIS method starting from the equations of the fluid model. To keep the notation light, we drop henceforth the explicit dependence on time of the domain and its subsets.

Following the derivation of the original ARIS method,[29] the left heart can be schematically outlined as a three-chambers domain as sketched in Figure 1: the Left Atrium (LA) $\Omega_{\text{LA}}$, the Left Ventricle (LV) $\Omega_{\text{LV}}$ and the Ascending

---

**ALGORITHM 1  Solution scheme for the Navier–Stokes equations in ALE formulation with the RIIS method for immersed surfaces**

Given the solution up to time $t^n$, to compute the solution at time $t^{n+1}$:

1: solve discretization of (1) to compute the domain displacement $\mathbf{d}^{n+1}$ and the domain $\Omega^{n+1}$

2: for each immersed surface $k \in \mathcal{I}_v$ do

3:    compute the opening coefficient $c_k^{n+1}$

4:    update the position of the immersed surface $\Gamma_k^{n+1}$ according to (3) and compute the signed distance function $\varphi_k^{n+1}$

5: **end for**

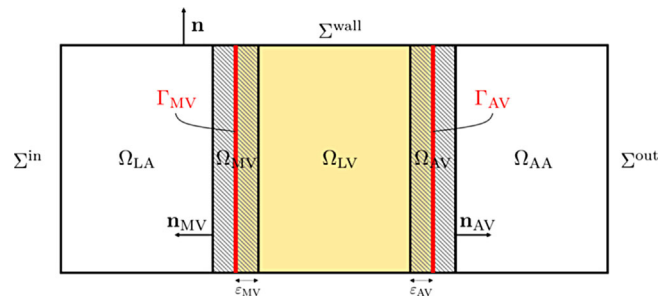6: solve discretized Navier–Stokes equations (4) to compute $\mathbf{u}^{n+1}$ and $p^{n+1}$

**FIGURE 1** Sketch of the three-chambers domain $\Omega$ with its subsets and boundaries. In yellow $\Omega_{LV}$, in white $\Omega_{LA}, \Omega_{AA}$, in striped pattern (partially overlapping $\Omega_{LV}, \Omega_{LA}, \Omega_{AA}$) the valve regions $\Omega_{MV}, \Omega_{AV}$. The latter are defined by the immersed surfaces $\Gamma_{MV}$ and $\Gamma_{AV}$ (in red) and the half-thicknesses $\varepsilon_k$, with $k \in \{MV, AV\}$.
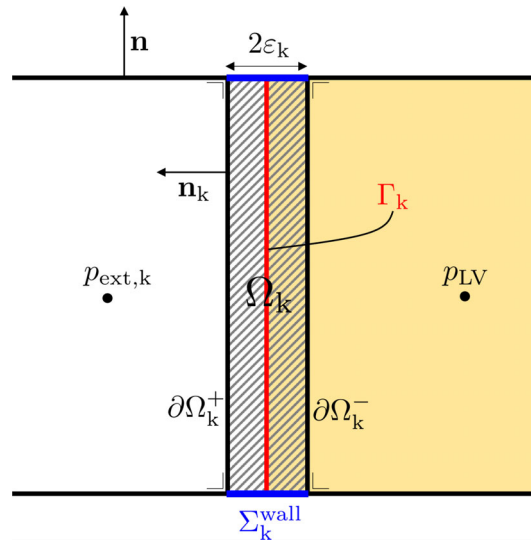


**FIGURE 2** Sketch of the immersed surface $\Gamma_k$ (red) with the corresponding valve region $\Omega_k$ (striped pattern) and its boundaries.

Aorta (AA) $\Omega_{AA}$. These chambers are separated by two surfaces representing the Mitral Valve (MV) $\Gamma_{MV}$ and the Aortic Valve (AV) $\Gamma_{AV}$, thus $\mathcal{I}_v = \{MV, AV\}$.

We denote by $\Omega$ the whole domain, such that $\overline{\Omega} = \overline{\Omega_{LA}} \cup \overline{\Omega_{LV}} \cup \overline{\Omega_{AA}}$. The domain boundary $\partial\Omega$ is partitioned into the inlet section $\Sigma^{in}$, the outlet section $\Sigma^{out}$ and the wall $\Sigma^{wall}$, as shown in Figure 1. We introduce the sets

$$\Omega_k = \left\{ \mathbf{x} \in \Omega : \text{dist}(\mathbf{x}, \Gamma_k) = \min_{\mathbf{y} \in \Gamma_k} \| \mathbf{x} - \mathbf{y} \| < \varepsilon_k \right\}, \quad k \in \{MV, AV\}, \tag{5}$$

where $\varepsilon_k$ is the half thickness of $\Omega_k$ (characterizing the RIIS method and already introduced in Section 2.1), banded in Figure 1, for $k \in \{MV, AV\}$. These regions have nontrivial intersections with the chambers defined above.

With reference to Figure 2, we introduce two geometric assumptions that will be used in the derivation of the augmented method of Section 2.2.

**Assumption 1.** (Flat valve surfaces) For $k \in \{MV, AV\}$, the normal vector $\mathbf{n}_k$ to the valve surface $\Gamma_k$ (pointing outwards w.r.t. $\Omega_{LV}$) is constant over $\Gamma_k$.

*Remark* 1. If Assumption 1 is satisfied, we can define a constant vector field extending the definition of the valve normal vector $\mathbf{n}_k$ to the whole valve region $\Omega_k$. We denote such field with the same symbol $\mathbf{n}_k : \Omega_k \to \mathbb{R}^3, k \in \{MV, AV\}$.

**Assumption 2.** (Valves orthogonal to the wall) By denoting with $\mathbf{n}$ the normal vector of $\partial\Omega$, $\mathbf{n}_k \cdot \mathbf{n} = 0$ on $\Sigma_k^{\text{wall}}$, for $k \in \{\text{MV}, \text{AV}\}$, where $\Sigma_k^{\text{wall}} = \Sigma^{\text{wall}} \cap \partial\Omega_k$.

*Remark* 2. By introducing $\partial\Omega_k^- = \partial\Omega_k \cap \Omega_{\text{LV}}$ and $\partial\Omega_k^+ = \partial\Omega_k \smallsetminus (\partial\Omega_k^- \cup \Sigma_k^{\text{wall}})$ (cfr. Figure 2) we observe that $|\partial\Omega_k^-| = |\partial\Omega_k^+| = |\Gamma_k|$, $k \in \{\text{MV}, \text{AV}\}$.

Moreover, we make the following assumptions:

**Assumption 3.** (Constant pressure in the compartments) Pressure is constant in space within $\Omega_{\text{LA}}$, $\Omega_{\text{LV}}$ and $\Omega_{\text{AA}}$. We will denote the respective constant values with $p_{\text{LA}}(t)$, $p_{\text{LV}}(t)$ and $p_{\text{AA}}(t)$.

**Assumption 4.** (Negligible inertia and viscosity within valves) For $k \in \{\text{MV}, \text{AV}\}$, inertial and viscous terms in (4a) are negligible in $\Omega_k$: $\mathcal{I}(\mathbf{u}) \approx \mathbf{0}$ and $\mathcal{D}(\mathbf{u}) \approx \mathbf{0}$.

When MV and AV are closed, the intraventricular pressure is prone to spurious oscillations, due to the ventricle being fully enclosed by boundaries on which a Dirichlet-type condition on the velocity is imposed (either strongly or through the RIIS penalty term). Thus, as done in Reference 29, we augment Equation (4) with a reaction term to impose $p_{\text{LV}}(t) = p^*(t)$, where $p^* : (0, T) \to \mathbb{R}$ is a prescribed value of the ventricular pressure (constant in space by Assumption 3). As for the ARIS method,[29] the ARIIS method assumes that the desired ventricular pressure $p^*(t)$ is known a priori. This information can be derived, for instance, from patient-specific experimental data. Alternatively, it can be provided by another mathematical model, such as an electromechanics simulation, as done in Reference 29 and in the present work.

We assume the perturbation term to be in the form[29]:

$$\sum_{k \in \{\text{MV}, \text{AV}\}} \mathcal{C}_k \delta_k \mathbf{n}_k, \tag{6}$$

with $\mathcal{C}_k \in \mathbb{R}$, for $k \in \{\text{MV}, \text{AV}\}$. This choice of the reaction term (6) is such that the augmented formulation acts on the valves only and does not perturb the momentum equation outside $\Omega_k$.

The perturbation term represents the force that the blood exerts on the closed valves during isovolumetric phases. We derive it to enforce that the ventricular pressure matches the reference one $p^*$. Thus, following,[29] we derive an estimation of the ventricular pressure $p_{\text{LV}}(t)$ when both valves are closed. The estimate will be used to determine the corrective term $\mathcal{C}_k$ in (6).

From (4a) and Assumption 4, we deduce[29]

$$\nabla p + \mathscr{R}(\mathbf{u}) = \mathbf{0} \quad \text{in } \Omega_k,$$

for all $k \in \{\text{MV}, \text{AV}\}$. Multiplying by $\mathbf{n}_k$[29] and integrating over $\Omega_k$, we get

$$\int_{\Omega_k} (\boldsymbol{\nabla} p + \mathscr{R}(\mathbf{u})) \cdot \mathbf{n}_k = 0.$$

By Assumption 1, we can take $\mathbf{n}_k$ out of the integral and integrate by parts the pressure term yielding

$$\left( \int_{\partial\Omega_k} p\mathbf{n} + \int_{\Omega_k} \mathscr{R}(\mathbf{u}) \right) \cdot \mathbf{n}_k = 0,$$

$$\int_{\partial\Omega_k} p\mathbf{n} \cdot \mathbf{n}_k + \int_{\Omega_k} \mathscr{R}(\mathbf{u}) \cdot \mathbf{n}_k = 0.$$

Using Assumptions 1 and 2, we get

$$\left(p_{\mathrm{LV}}-p_{\mathrm{ext},k}\right)|\Gamma_k|-\int_{\Omega_k}\mathscr{R}(\mathbf{u})\cdot\mathbf{n}_k=0, \tag{7}$$

where, $p_{\mathrm{ext},k}=p_{\mathrm{LA}}$ for $k=\mathrm{MV}$ and $p_{\mathrm{ext},k}=p_{\mathrm{AA}}$ for $k=\mathrm{AV}$. Finally, summing (7) for both valves,[29] we obtain:

$$\left(p_{\mathrm{LV}}-p_{\mathrm{LA}}\right)|\Gamma_{\mathrm{MV}}|+\left(p_{\mathrm{LV}}-p_{\mathrm{AA}}\right)|\Gamma_{\mathrm{AV}}|-\sum_{k\in\{\mathrm{MV},\mathrm{AV}\}}\int_{\Omega_k}\mathscr{R}(\mathbf{u})\cdot\mathbf{n}_k=0, \tag{8}$$

from which we derive

$$p_{\mathrm{LV}}=\frac{1}{|\Gamma_{\mathrm{MV}}|+|\Gamma_{\mathrm{AV}}|}\left(|\Gamma_{\mathrm{MV}}|p_{\mathrm{LA}}+|\Gamma_{\mathrm{AV}}|p_{\mathrm{AA}}+\sum_{k\in\{\mathrm{MV},\mathrm{AV}\}}\int_{\Omega_k}\mathscr{R}(\mathbf{u})\cdot\mathbf{n}_k\right). \tag{9}$$

Repeating these calculations including the perturbation term (6), (8) rewrites as

$$\sum_{k\in\{\mathrm{MV},\mathrm{AV}\}}\left(\left(p_{\mathrm{LV}}-p_{\mathrm{ext},k}\right)|\Gamma_k|-\int_{\Omega_k}\mathscr{R}(\mathbf{u})\cdot\mathbf{n}_k-\mathcal{C}_k\int_{\Omega_k}\delta_k\right)=0,$$

so that, if the perturbation satisfies

$$\sum_{k\in\{\mathrm{MV},\mathrm{AV}\}}\int_{\Omega_k}\mathcal{C}_k\delta_k=\sum_{k\in\{\mathrm{MV},\mathrm{AV}\}}\left(\left(p^*-p_{\mathrm{ext},k}\right)|\Gamma_k|-\int_{\Omega_k}\mathscr{R}(\mathbf{u})\cdot\mathbf{n}_k\right), \tag{10}$$

then our estimate for $p_{\mathrm{LV}}$ becomes $p_{\mathrm{LV}}=p^*$.

Equation (10) admits infinitely many solutions for the perturbation terms $\mathcal{C}_{\mathrm{MV}}$ and $\mathcal{C}_{\mathrm{AV}}$. In analogy with[29], we choose a solution such that the correction due to spriouos flow through the immersed surfaces is distributed equally between MV and AV. Observing that $\int_{\Omega_k}\delta_k=|\Gamma_k|$, the chosen corrective term reads:

$$\mathcal{C}_k(\mathbf{u},p)=p^*-p_{\mathrm{ext},k}-\frac{1}{|\Gamma_{\mathrm{MV}}|+|\Gamma_{\mathrm{AV}}|}\sum_{k\in\{\mathrm{MV},\mathrm{AV}\}}\int_{\Omega_k}\mathscr{R}(\mathbf{u})\cdot\mathbf{n}_k. \tag{11}$$

Thus, the ARIIS method consists in solving the following problem:

$$\begin{cases} \rho\left(\dfrac{\partial\mathbf{u}}{\partial t}+((\mathbf{u}-\mathbf{u}_{\mathrm{ALE}})\cdot\boldsymbol{\nabla})\mathbf{u}\right)-\boldsymbol{\nabla}\cdot\left(\mu(\boldsymbol{\nabla}\mathbf{u}+\boldsymbol{\nabla}^T\mathbf{u})\right)+\boldsymbol{\nabla}p \\ \quad +\displaystyle\sum_{k\in\{\mathrm{MV},\mathrm{AV}\}}\left(\dfrac{R_k}{\varepsilon_k}\delta_k(\varphi_k)(\mathbf{u}-\mathbf{u}_{\mathrm{ALE}}-\mathbf{u}_{\Gamma_k})+\chi_{\mathrm{iso}}(t)\mathcal{C}_k(\mathbf{u},\,p)\delta_k\mathbf{n}_k\right)=0 & \text{in }\Omega\times(0,T),\ (a) \\ \boldsymbol{\nabla}\cdot\mathbf{u}=0 & \text{in }\Omega\times(0,T),\ (b) \end{cases} \tag{12}$$

endowed with suitable initial and boundary conditions. $\chi_{\mathrm{iso}}(t)$ is a characteristic function equal to 1 during the iso-volumetric phases, 0 otherwise: we activate the ARIIS correction term only when both valves are simultaneously closed. $\chi_{\mathrm{iso}}(t)$ can be prescribed a priori or be determined by pressure jump conditions (to determine the opening and closing of valves).[29]

*Remark* 3. For the derivation of the ARIIS method, we follow a methodology analogous to the one introduced for the derivation of the original ARIS method.[29] In particular, our derivation differs from the ARIS[29] one for the following aspects.

- The ARIS method[29] is derived starting from an interface stress jump condition on the immersed surface $\Gamma_k$. This is not applicable in the case of RIIS[65] (and ARIIS) method. Indeed, the valves are here distributed inside bulk layers around the immersed surfaces. Thus, we carry out all the integrations in volumes ($\Omega_k$) instead of surfaces ($\Gamma_k$).
- We do not need the incompressibility constraint in the derivation.
- The geometrical assumptions 1 and 2 are not needed in the ARIS method[29] since the integrals are defined on the immersed surface.

Of the assumptions used in the derivation of ARIIS, Assumption 4 holds for $R$ large enough, that is consistent with $R$ being the penalty coefficient for the kinematic condition on the valve, whereas the other three are instrumental in simplifying the derivation of the augmenting term (6). In particular, the violation of Assumptions 1 and 2 would require this corrective term to account for detailed geometric properties of the valve leaflet (e.g., its curvature distribution). Assumption 3 instead could be slightly relaxed without having to modify the derivation, by assuming that pressure is homogeneous only on each $\partial\Omega_k^+$ and $\partial\Omega_k^-$, separately (and not within the chambers). This would require the evaluation of pressure on surfaces not conforming to the mesh. Nonetheless, the numerical tests of Sections 3.2 and 3.3 will show that pressure is indeed substantially constant within each chamber (during the isovolumetric phases), and that the proposed correction term can be used successfully also in cases in which some of the assumptions are not exactly verified.

## 2.2.1 | Numerical approximation

Spatial discretization follows that used in the RIIS method (see Section 2.1.1). The temporal discretization scheme is modified to compute the ARIIS correction term. At every time $t^{n+1}$, the correction term is computed in an explicit way, that is, using the valve configuration and fluid velocity from the previous time step, as shown in Algorithm 2.

## 3 | NUMERICAL RESULTS

In this section, we present and discuss the results on the ARIIS method by carrying out numerical simulations of three different problems. All three tests feature valves that open and close. In Section 3.1, we check the validity of our method by considering the simple problem introduced in Reference 29 (Test A). In Section 3.2, we propose a new benchmark problem consisting of the flow in a compliant pipe with ventricle-like shortening (Test B). Finally, in Section 3.3, we apply our method to a cardiac case, that is, the flow in a realistic left heart geometry (Test C).

The physical parameters for blood are density $\rho = 1.06 \times 10^3 \text{kg/m}^3$ and dynamic viscosity $\mu = 3.5 \times 10^{-3} \text{kg/(m s)}$. In all the numerical experiments considered, we apply a null velocity initial condition. Furthermore, similarly to

---

**ALGORITHM 2**    **Solution scheme for the Navier–Stokes equations in ALE formulation with the ARIIS method**

```
Given the solution up to time tⁿ, to compute the solution at time tⁿ⁺¹:
1: solve discretization of (1) to compute the domain displacement dⁿ⁺¹ and the domain Ωⁿ⁺¹
2: for k∈𝓘ᵥ do
3:      if χ_iso(tⁿ⁺¹)=1 then
4:          compute 𝒞ₖⁿ⁺¹=𝒞ₖ(uⁿ,pⁿ)
5:      end if
6:      compute cₖⁿ⁺¹
7:      update Γₖⁿ⁺¹
8: end for
9: solve discretized Navier-Stokes equations (4) to compute uⁿ⁺¹ and pⁿ⁺¹
```

References 21,30, we use a quasi-static approach by choosing $\mathbf{u}_{\Gamma_k} = \mathbf{0}$, that is, we neglect the velocity with which valves move when changing configuration.

We discretize (12) in space with piecewise linear Finite Elements (FE) for velocity and pressure ($\mathbb{P}_1 - \mathbb{P}_1$) and in time with the backward Euler method. We employ a semi-implicit treatment of the non-linear term. In Sections 3.1 and 3.2, we use a SUPG-PSPG stabilization.[81] Differently, in Section 3.3, we use the VMS-LES method acting as both a stabilization method and a turbulence model to account for the transition-to-turbulence flow regime typically occurring in cardiac flows.[16,82,83]

The lifting problem (1) is discretized with linear FEs. Moreover, in the first two test cases, we set $\psi = 1$ for all $\mathbf{x} \in \Omega_0$, so Equation (1) becomes a simple Laplacian problem. Differently, in Test C, to avoid mesh elements distortion, we use the boundary-based stiffening approach proposed in Reference 84. In this method, we define $\psi$ as[84]

$$\psi(\mathbf{x}) = \max\left(d(\mathbf{x}), \alpha\right)^{-\beta} \text{ in } \Omega_0,$$

where $d$ is the distance from the boundary, $\alpha$ and $\beta$ are two parameters that we set equal to $\alpha = 0$ and $\beta = 1$.

We carry out our numerical simulations in `life`[x],[85,86*] a high-performance C++ FE library developed within the iHEART project,[**] mainly focused on cardiac simulations and based on the `deal.II` finite element core.[87–89] The source code of the `life`[x] module for hemodynamics simulations, referred to as `life`[x]`-cfd`, has been recently released.[90,91]

## 3.1 | Test A: a simple benchmark problem

In this section, following,[29] we consider a benchmark problem that was originally introduced to test the ARIS method in a simplified setting.

The domain is a cylinder of radius $R_c = 0.01$ m and length $L_c = 0.1$ m. It is divided into three cylindrical compartments, representing, in an idealized context, the LA, LV and AA, of lengths $L_{LA} = 0.02$ m, $L_{LV} = 0.06$ m and $L_{AA} = 0.02$ m, respectively. Two planar surfaces represent the MV and AV. We solve in the time interval $[0, T]$, with $T = 0.2$ s.

The domain is discretized with a tetrahedral mesh of 75,933 elements, for a total of 56,684 degrees of freedom. The mesh is finer near to the immersed surfaces, to better capture their presence, with a minimum element diameter $h_{min} = 1$ mm and a maximum diameter $h_{max} = 4.6$ mm (see Figure 3). Simulations ran in parallel using 4 cores of a local workstation, each with an Intel Core i5-9600K@3.70 GHz processor.

Following Reference 29, we impose a homogeneous and constant pressure of $p_{in} = 0$ mmHg at the inlet section, and a homogeneous and constant pressure of $p_{out} = 75$ mm Hg at the outlet section. The displacement $\mathbf{d}_{\partial\Omega}$ of the lateral boundary is prescribed analytically and mimics the contraction-relaxation cycle of a human ventricle. For a given point $\mathbf{x} = (x_1, x_2, x_3)^T$ and time $t$, it is defined as
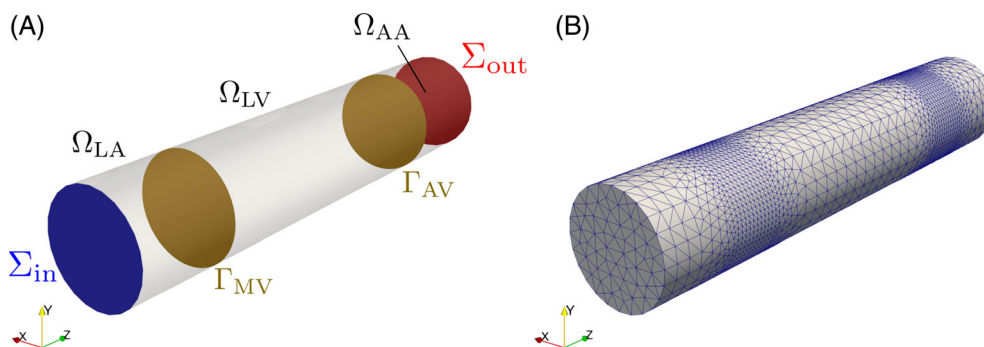


**FIGURE 3** Test A. Domain for the cylinder test cases, with highlighted immersed and boundary surfaces (A); tetrahedral mesh for the cylinder test cases.

$$\mathbf{d}_{\partial\Omega}(\mathbf{x},t) = \begin{cases} \overline{w}A(t)\mathbf{e}_r(\mathbf{x})\exp\left(-\dfrac{\left|x_3 - \frac{L_c}{2}\right|^2}{2\sigma^2}\right) & \text{if } x_3 \in [L_{LA}, L_{LA} + L_{LV}), \\ \mathbf{0} & \text{otherwise,} \end{cases}$$

with

$$\mathbf{e}_r(\mathbf{x}) = \frac{(x_1, x_2, 0)^T}{\sqrt{x_1^2 + x_2^2}}.$$

$A(t)$ is the piecewise linear function depicted in Figure 4A. We set $\sigma = 0.015$ and $\overline{w} = 4.6 \times 10^{-4}$ m, to have the same time evolution of volume as in 29 (see Figure 4B).

We simulate the opening of a valve by instantaneously removing the corresponding surface from the domain. This choice is consistent with the setting proposed in Reference 29. Valves are opened and closed at prescribed times, following the evolution of the volume of the ventricular compartment: when the volume is increasing, the MV is open and the AV is closed; when it is decreasing, the MV is open and the AV is closed; when the volume is constant, both valves are closed. The MV is closed when the simulation starts, while the AV is open. Closing and opening times are reported in Figure 4B.

In this setting, we carry out a comparison of the results obtained with the RIIS method against those obtained with the ARIIS method, using as reference pressure $p^*(t)$ a piecewise linear function. The evolution of ventricular pressure for both cases, computed with resistance $R = 10^4$ kg/(m s) and $\varepsilon = 0.002$ m, is reported in Figure 5. The plots show how the ARIIS method allows the ventricular pressure to accurately follow the provided reference pressure. Differently, the pressure computed by the RIIS method is nonphysical: it remains constant for the overall duration of the isovolumetric phases—instead of decreasing or increasing—and it is equal to the average pressure between the upwind and the downwind chambers. The same trend is also observed in the original ARIS method.[29] We believe that this behavior can be explained by the simplified setting characterizing this specific benchmark problem: the domain is symmetric and, during the isovolumetric phases, the prescribed displacement is null. Furthermore, the observed peaks are associated to the simplified and instantaneous way in which valves are opened and closed and to the explicit computation of the corrective term (6).

Moreover, we carry out a sensitivity analysis by varying the resistance coefficient $R$ in the ARIIS method, to understand how the quality of the results is influenced by it. Results are reported in Figure 6. Although the resistance coefficient varies by several orders of magnitude, no difference is observed on the accuracy of the ventricular pressure. This is evident in particular in Figure 6B, reporting the relative pressure error
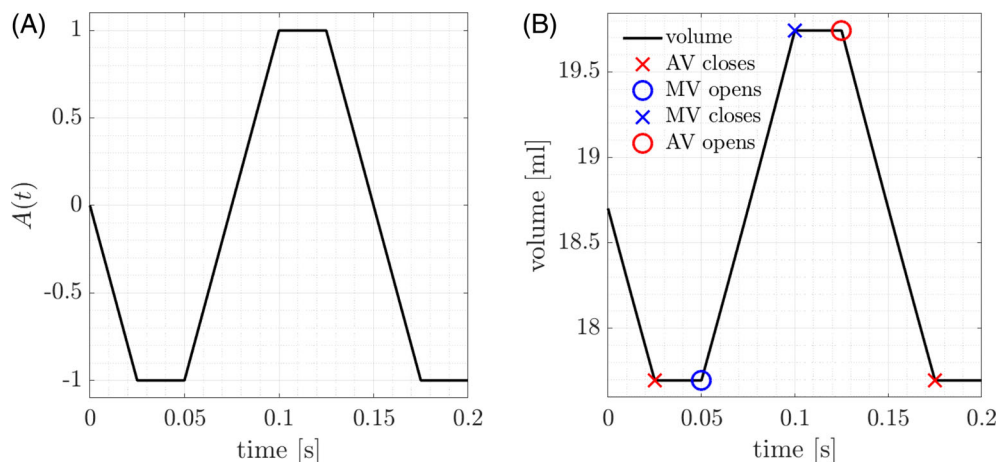


**FIGURE 4** Test A. (A) Plot of the function $A(t)$ that defines the time evolution of the boundary displacement in the cylindrical toy problem. (B) The corresponding volume of the ventricular compartment with valve opening and closing times.
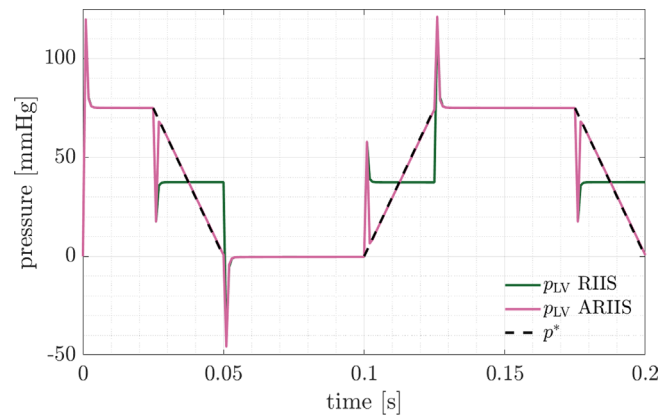
**FIGURE 5**   Test A. Ventricular and reference pressures for the cylindrical toy problem, with RIIS and ARIIS methods, using resistance $R = 10^4$ kg/(m s) and $\varepsilon = 0.002$ m.
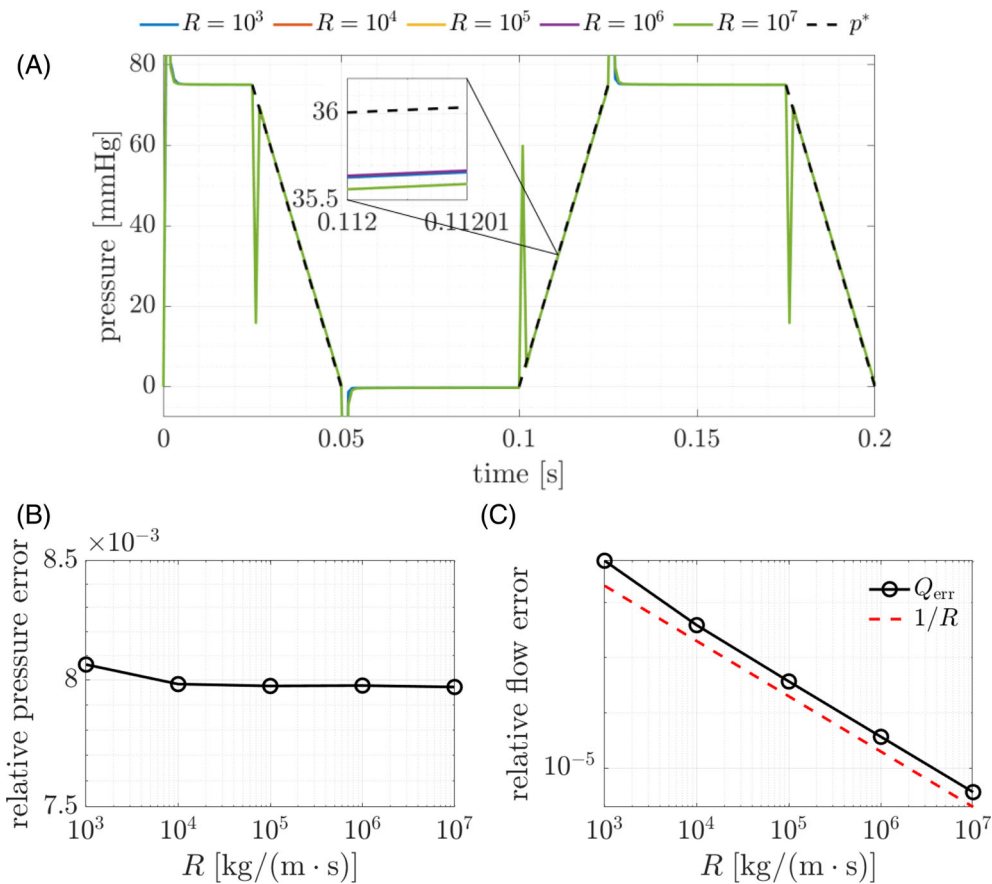


**FIGURE 6**   Test A. (A) Evolution of pressure with the ARIIS method with varying values of the resistance. (B) Relative error between the computed pressure during isovolumic phases and the reference pressure $p^*$.

$$\frac{\max_{t \in T_{\mathrm{iso}}} |p_{\mathrm{LV}} - p^*|}{\max_{t \in T_{\mathrm{iso}}} |p^*|}, \tag{13}$$

where, $T_{\mathrm{iso}} = \{t \in (0, T) : \chi_{\mathrm{iso}}(t) = 1\}$ is the set of times at which both valves are closed. The error is approximately equal to $8 \times 10^{-3}$ regardless of the value of $R$. The ARIIS method, therefore, yields reliable pressure results also with high

values of $R$, that ensure negligible spurious flow through the resistive surfaces. We found that, above the threshold $\varepsilon \geq 1.5h$ (see Section 2.1.1), the results are substantially independent of $\varepsilon$.

We can assess the effectiveness of the ARIIS method also in terms of spurious flow through the closed valve. In Figure 6C, we plot the relative flowrate error through the MV, evaluated as

$$\frac{\max_{t \in T_{\text{iso}}} | Q_{\text{MV}} |}{\max_{t \in (0,T)} | Q_{\text{MV}} |}.$$

We can observe that, as $R \rightarrow \infty$, the spurious flow tends to zero with order 1, confirming the effectiveness of the penalization.

Overall, the obtained results indicate that the ARIIS method is successful in its aim of producing a ventricular pressure that closely follows the prescribed reference evolution.

## 3.2 │ Test B: a benchmark problem including ventricular shortening

As an intermediate step towards cardiac simulations, we introduce a novel test case in a cylindrical domain that mimics the ventricular shortening during contraction. We use the same domain as in Section 3.1, but change the boundary displacement as follows:

$$\mathbf{d}_{\partial\Omega}(\mathbf{x},t) = \begin{cases} \mathbf{0} & \text{if } x_3 \in [0,L_{\text{LA}}), \\ \mathbf{d}_{\partial\Omega}^r(\mathbf{x},t) + \mathbf{d}_{\partial\Omega}^z(\mathbf{x},t) & \text{if } x_3 \in [L_{\text{LA}}, L_{\text{LA}}+L_{\text{LV}}), \\ \left(0, \ 0, \ L_{\text{LV}}^*(t) - L_{\text{LV}}\right)^T & \text{if } x_3 \in [L_{\text{LA}}+L_{\text{LV}}, L), \end{cases} \tag{14}$$

with

$$\mathbf{d}_{\partial\Omega}^r(\mathbf{x},t) = \left( R_c + c(t)\sin\left(\frac{\pi(x_3 - L_{\text{LA}})}{L_{\text{LV}}}\right) \right)\mathbf{r}(\mathbf{x}) - \mathbf{x}, \tag{15}$$

$$\mathbf{d}_{\partial\Omega}^z(\mathbf{x},t) = \frac{x_3 - L_{\text{LA}}}{L_{\text{LV}}}\left(L_{\text{LV}}^*(t) - L_{\text{LV}}\right), \tag{16}$$

and

$$c(t) = \frac{4R_c}{\pi} + \frac{\sqrt{16R_c^2 L_{\text{LV}}^*(t)^2 - 2\pi L_{\text{LV}}^*(t)\left(\pi L_{\text{LV}}^*(t)R_c^2 - V_{\text{LV}}^*(t)\right)}}{\pi L_{\text{LV}}^*(t)}. \tag{17}$$

In the above, $L_{\text{LV}}^*(t)$ and $V_{\text{LV}}^*(t)$ are prescribed time dependent functions for the ventricular length and volume, respectively. The displacement is such that, at any time $t$, the ventricular length and volume in the deformed configuration match the prescribed ones. We take $\psi = 1$ in (1). Valve positions change over time following the domain displacement. Their opening and closing times, determined a priori following the same rule as in Section 3.1, are reported in Figure 7. The MV starts open, and the AV starts closed. Moreover, we set inlet and outlet boundary conditions to $p_{\text{in}} = 0$ mmHg and $p_{\text{out}} = 80$ mmHg, to replicate the typical range that characterizes the heart function. We remark that the assumptions of the ARIIS derivation are not exactly satisfied by this test case: therefore, the test verifies the robustness of the method with respect to the violation of its assumptions.

Numerical simulations are run in parallel on the GALILEO100 supercomputer[†] at the CINECA supercomputing center, using 48 cores.

Figures 8 and 9 report snapshots of pressure and velocity in the solution, computed using RIIS and ARIIS. We can observe that the two methods yield equivalent results outside the isovolumetric phases. Differently, when both valves are closed, a considerably different pressure can be observed. Similar conclusions can be drawn from the plots reported
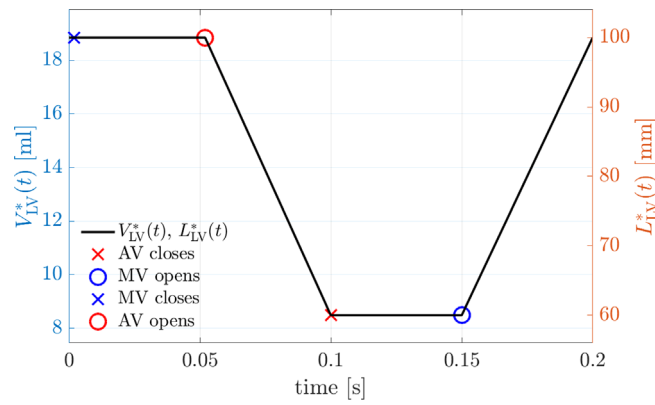
**FIGURE 7**    Test B. Prescribed ventricular volume $V_{LV}^*(t)$ (left axis) and length $L_{LV}^*(t)$ (right axis).
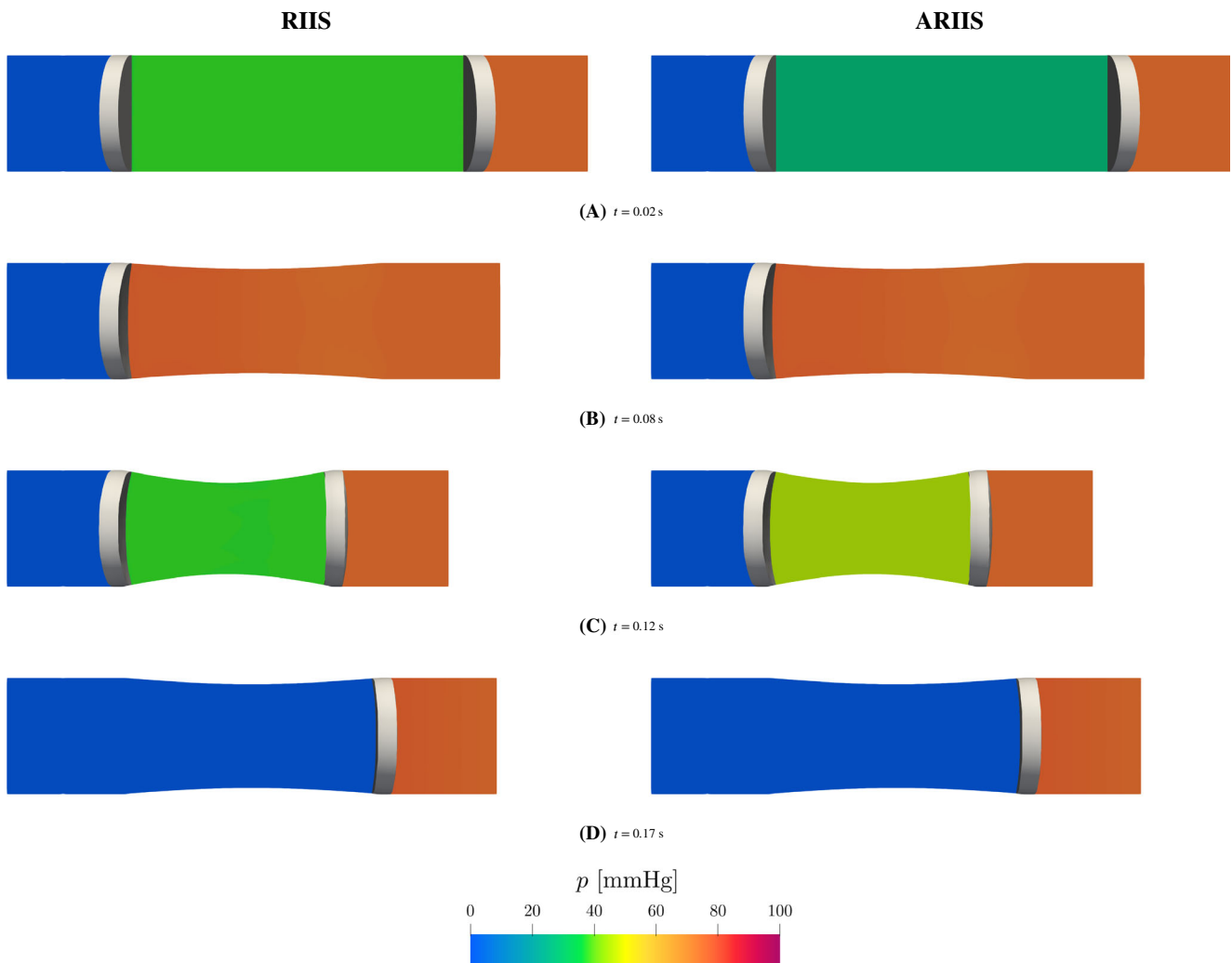


**FIGURE 8**    Test B. Snapshots of the pressure over one longitudinal slice of the domain, simulated using the RIIS (left) and ARIIS (right) method. The snapshots are taken at the midpoint of isovolumetric contraction (A), ejection (B), isovolumetric relaxation (C), and filling (D). The domain is warped according to the displacement **d** defined in (14).

in Figure 10, representing the average ventricular pressure over time for Test B, using RIIS and ARIIS, setting $R = 10^4$ kg/(m s) and $\varepsilon = 0.002$ m. The ARIIS simulation yields a pressure that closely follows the provided reference pressure $p^*$ during isovolumetric phases. Conversely, outside the isovolumetric phases, the two methods correctly produce

**RIIS**                                    **ARIIS**



**(A)** $t = 0.02$ s

**(B)** $t = 0.08$ s

**(C)** $t = 0.12$ s

**(D)** $t = 0.17$ s

$|\mathbf{u}|$ [m/s]

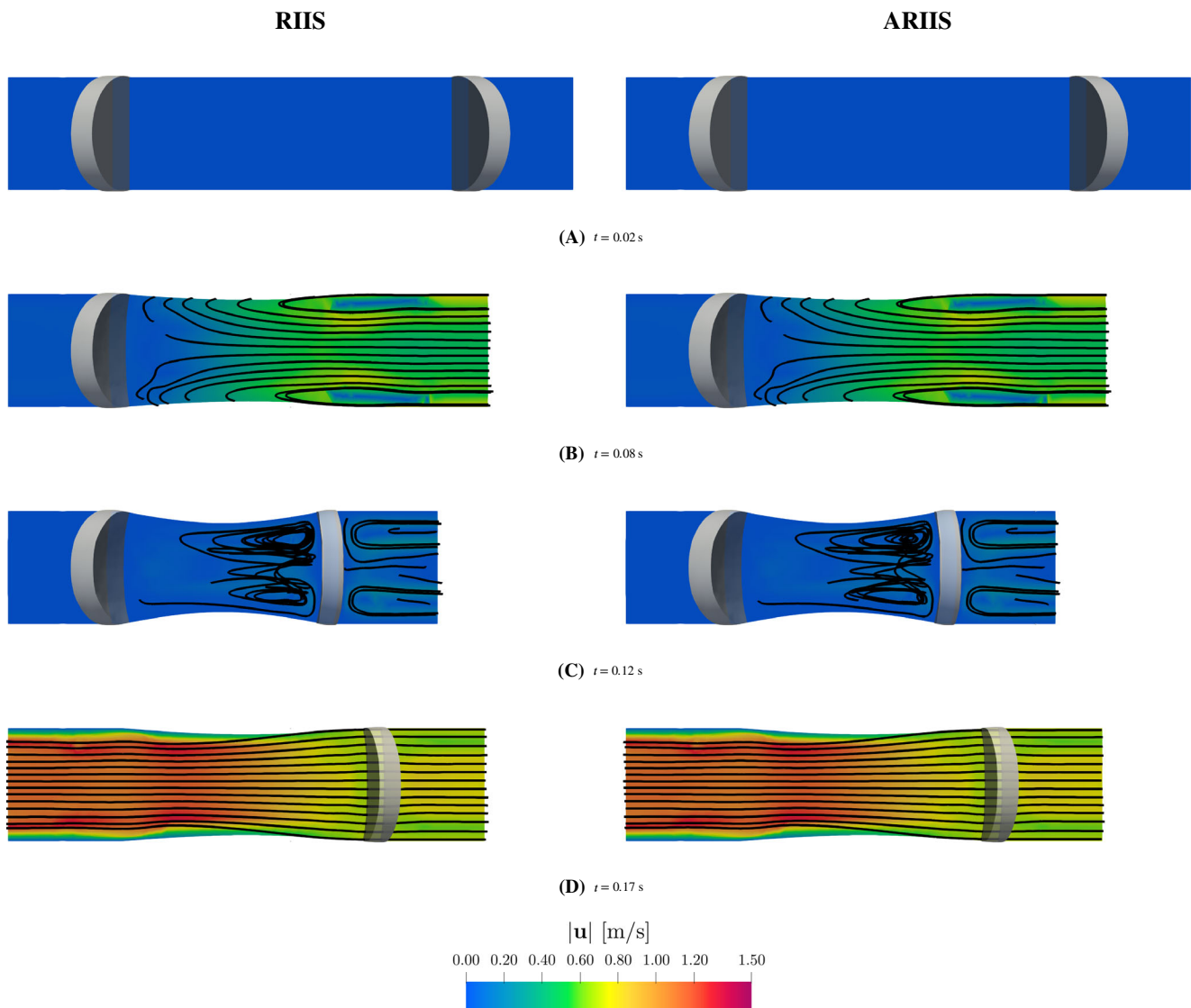0.00  0.20  0.40  0.60  0.80  1.00  1.20     1.50

**FIGURE 9**    Test B. Snapshots of the velocity magnitude over one longitudinal slice of the domain, simulated using the RIIS (left) and ARIIS (right) methods. The snapshots are taken at the midpoint of isovolumetric contraction (A), ejection (B), isovolumetric relaxation (C), and filling (D). The domain is warped by the displacement $\mathbf{d}$ defined in (14), and the velocity magnitude is superimposed with the streamlines of the flow field.

the same result. Figure 11 highlights the solution on one of the valves during the isovolumetric relaxation phase: with both the RIIS and ARIIS methods, the spurious flow across the valve is negligible (the peak velocity is three orders of magnitude smaller than the peak velocity throughout the simulation), and the resistive term results in a pressure gradient across the valve.

We carry out numerical simulations with the ARIIS method by varying the resistance coefficient $R$ over several orders of magnitude and computing the relative pressure error (13) during isovolumetric phases. We report the results in Figure 12. As before, we observe that the reference pressure is matched accurately during isovolumetric phases, regardless of the value of $R$.

## 3.3 | Test C: application to a cardiac test case

In this section, we apply the ARIIS method to a realistic cardiac case. We use the CFD model of a healthy left heart developed in Reference 30. It consists of the 3D fluid dynamics model (12) coupled to the surrounding circulation (described by a 0D closed-loop model[92–94]) and driven by a cardiac electromechanical model.[94]
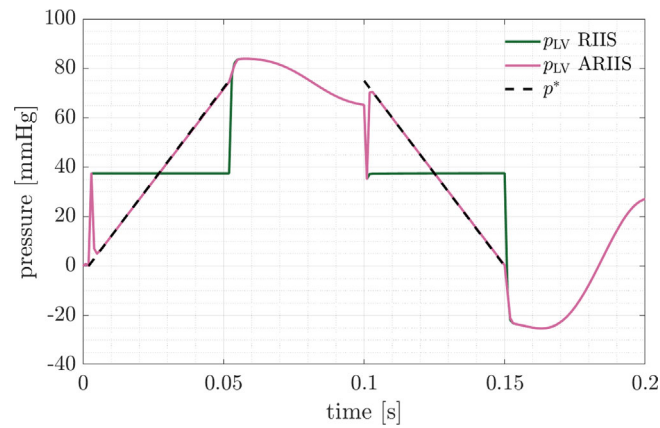
**FIGURE 10** Test B. Ventricular and reference pressures, with RIIS and ARIIS methods, using resistance $R = 10^4$ kg/(m s) and $\varepsilon = 0.002$ m.
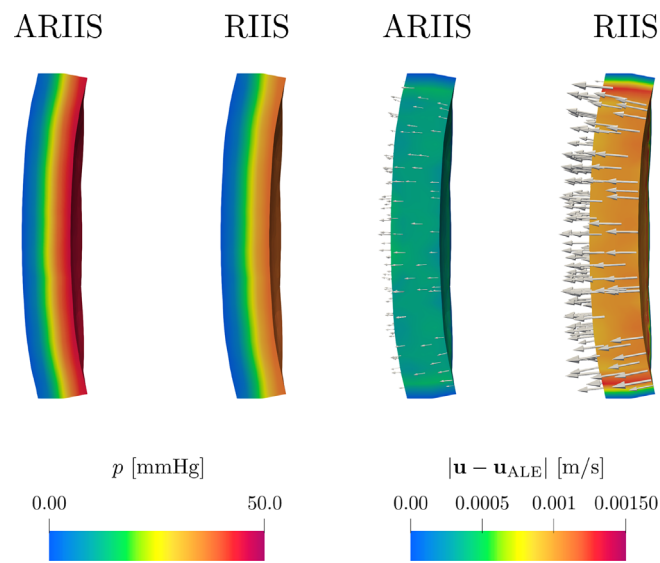


**FIGURE 11** Test B. Longitudinal clip of the solution of within the MV, with the ARIIS and RIIS methods, at time $t = 0.12$ s (i.e., during the isovolumetric relaxation phase). Left: pressure, right: magnitude of the relative velocity $\mathbf{u} - \mathbf{u}_{ALE}$.

We consider a realistic left heart geometry provided by Zygote,[95] representing an accurate 3D model of the heart obtained with CT scan data. We report the domain in Figure 13A: its boundary is split as $\partial\Omega = \Sigma^{in} \cup \Sigma^{out} \cup \Sigma_t^{wall}$, where $\Sigma^{in}$ is the set of pulmonary veins inlet sections, $\Sigma^{out}$ the outlet section of the ascending aorta and $\Sigma_t^{wall}$ the wall (endocardium). In addition, we display the immersed surfaces $\Gamma_{MV}$ and $\Gamma_{AV}$ in their closed configurations. As observed for Test B in Section 3.2, the assumptions of the ARIIS method are not exactly satisfied in this case, and the test verifies how the method behaves when assumptions are violated.

We set Neumann boundary conditions on the inlet and outlet sections of the domain by prescribing the pressure coming from the coupling between the 3D and the 0D circulation model, as explained in Reference 16. To prescribe the displacement field on the endocardium of the LV, we carry out an electromechanical simulation with the ventricular model proposed in Reference 94, consisting of a 3D electromechanical model fully-coupled to the external 0D circulation. In the electromechanical simulation, the AV and MV are modeled as non-ideal diodes that change their state instantaneously.

We report the complete setup of the electromechanical model in Appendix A. Moreover, since the focus of the article is the correct estimation of the ventricular pressure only, we neglect the motion of the remaining part of the domain by setting homogeneous Dirichlet boundary conditions on the wall of the left atrium and the ascending aorta.
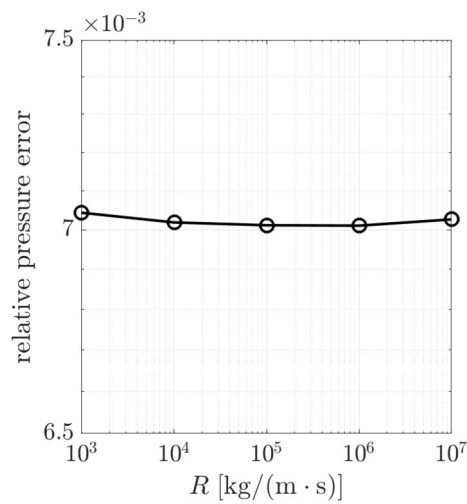
**FIGURE 12**    Relative error between the computed pressure during isovolumetric phases and the reference pressure $p^*$, with varying resistance $R$, $\varepsilon = 0.002$ m and minimum mesh size $h_{\min} = 0.001$ m.
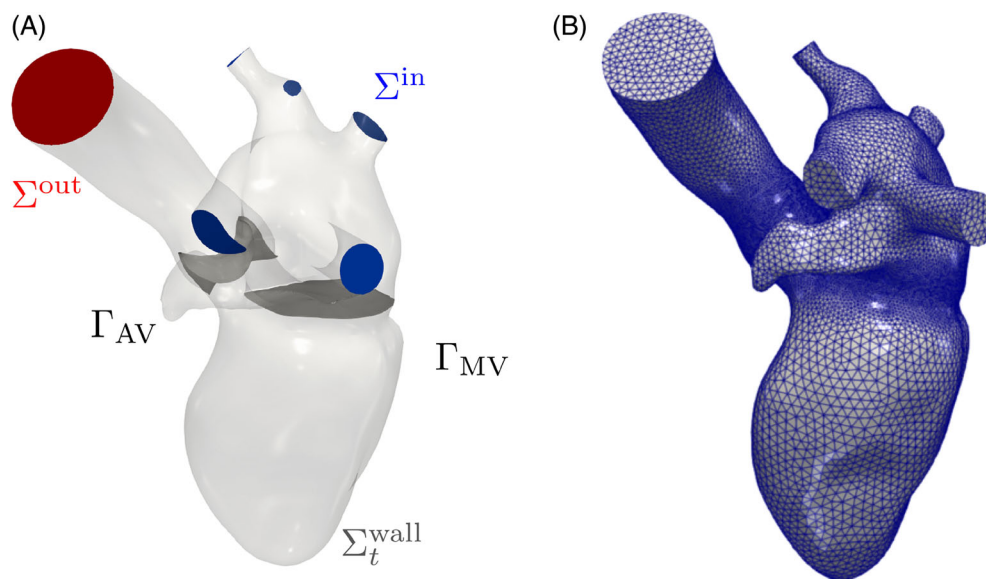


**FIGURE 13**    Test C. Left heart CFD domain highlighting boundary portions and immersed surfaces in their closed configurations (A); tetrahedral mesh generated for the CFD simulation (B).

**TABLE 2**    Test C. Mesh details for the left heart CFD simulations.

| $h$ (mm) | | | | DOFs ($\mathbb{P}_1 - \mathbb{P}_1$) (−) | | | |
|---|---|---|---|---|---|---|---|
| **Min** | **Avg** | **Max** | **Cells (−)** | **u** | **p** | | **Total** |
| 0.44 | 1.44 | 6.40 | 645,699 | 333,243 | 111,081 | | 444,324 |

We generate the tetrahedral mesh of the left heart displayed in Figure 13B with vmtk[96] using the methods and tools discussed in References 30,97. Mesh details are summarized in Table 2. We use as time-step size $\Delta t = 2.5 \times 10^{-4}$ s. Since the electromechanical simulation has a much larger timestep than the CFD one, we use smoothing splines[98] to approximate the electromechanical displacement field in time.

The values of $R_k$ and $\varepsilon_k$ of the RIIS method are provided in Table 3. These values of $\varepsilon_k$ and $R_k$ prevent flow through the closed immersed surfaces.[65] Moreover, following,[65] we choose $\varepsilon_k$ to guarantee that $\varepsilon_k \geq 1.5 h_{\min}$, where $h_{\min}$ is the

minimum mesh size in the valves region. Since the condition number of the linear system associated to the FE discretization of (12) increases as the ratio $R_k/\varepsilon_k$ increases, we choose the minimum value of $R_k$ that guarantees impervious valves, as in Reference 30. In Table 3, we also report the areas of the valve sections needed for the ARIIS method. Moreover, as reference pressure $p^*(t)$, we use the one computed in the 3D-0D electromechanical ventricular model.[94]

Numerical simulations are run in parallel using 48 cores from the GALILEO100 supercomputer at the CINECA supercomputing center.

### 3.3.1 | Comparison of RIIS and ARIIS methods

We carry out numerical simulations with the RIIS and the ARIIS methods. We simulate a single heartbeat of period $T = 0.8$ s. In Figure 14, we display the LV volume with the four heartbeat phases, along with the times corresponding to the begin and end of isovolumetric phases. Consistently with the electromechanical simulation, the valves open and close instantaneously (i.e., they switch between the open and closed configurations over a single time step), according to the evolution of ventricular volume, following the same criterion as in Section 3.1. The opening and closing times are reported in Figure 14 and Table 3. As reference pressure ($p^*$) for the ARIIS method, we use the LV pressure coming from the 3D cardiac electromechanical simulation coupled to the 0D cardiocirculatory model.[94]

We display the ventricular pressure with the RIIS and ARIIS methods in Figure 15. We compute it by space-averaging the pressure in a control volume downstream of the MV. The RIIS method is not able to correctly capture the left ventricular pressure, yielding arbitrary pressure values during the isovolumetric phases, with unphysical oscillations. Differently, with the correction term introduced by the ARIIS method, the ventricular pressure follows the expected trend given by $p^*$. In addition, out of the isovolumetric phases, the pressure fields are almost identical between

**TABLE 3**  Test C. Parameters of the RIIS and ARIIS methods in the left heart CFD simulations.

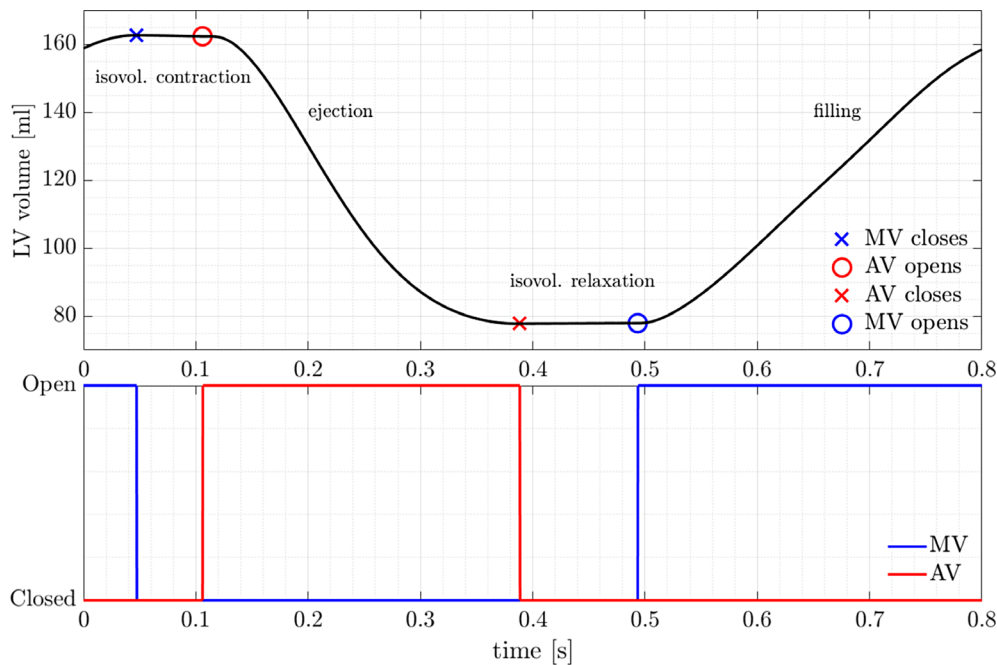| $k$ | $R_k$ (kg/(m s)) | $\varepsilon_k$ (mm) | $\|\Gamma_k\|$ (cm$^2$) | Clos. time (s) | Open. time (s) |
|-----|------------------|----------------------|--------------------------|----------------|----------------|
| MV  | $1 \times 10^4$  | 1.0                  | 12.11                    | 0.04725        | 0.49350        |
| AV  | $1 \times 10^4$  | 1.0                  | 5.41                     | 0.38850        | 0.10600        |



**FIGURE 14**  Test C. Volume of left ventricle, with opening and closing times for valves, and valve states.

RIIS and ARIIS methods. Indeed, the correction term is active in the isovolumetric phases only, and it does not influence the remaining phases of the heart cycle, yielding a maximum discrepancy of 0.23 mmHg.

Furthermore, as shown in Figure 16, the largest discrepancies between $p_{LV}$ and $p^*$ in the ARIIS case are attained at the end of the isovolumetric phases. These discrepancies are related to the fact that the isovolumetric phases in realistic cardiac simulations are not exactly volume preserving. This happens due to, on the one hand, the projection of the displacement from the electromechanics (or imaging data) onto the fluid dynamics mesh and, on the other hand, the lifting problem in (1) that does not guarantee, a priori, any kind of volume conservation in the LV subdomain. Moreover, the displacement is characterized by small oscillations in time—introduced by the smoothing splines—that yield oscillations in the ventricular volume as well. Nonetheless, differently from the standard RIIS method, the proposed
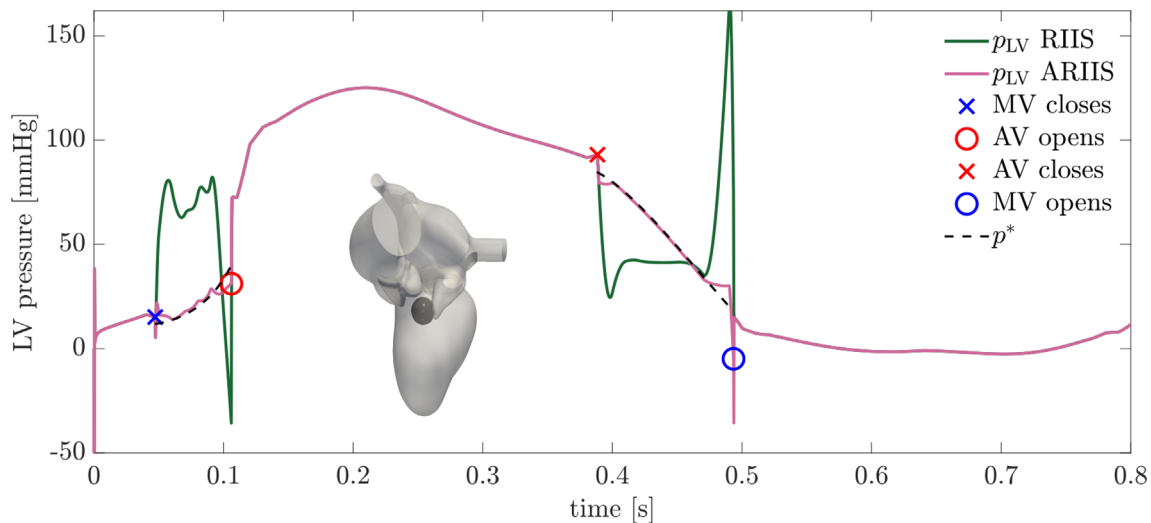


**FIGURE 15** Test C. Ventricular and reference pressures for the left heart test case, with RIIS and ARIIS methods. $p_{LV}$ is computed space-averaging the fluid pressure in the black control volume in the left ventricle.
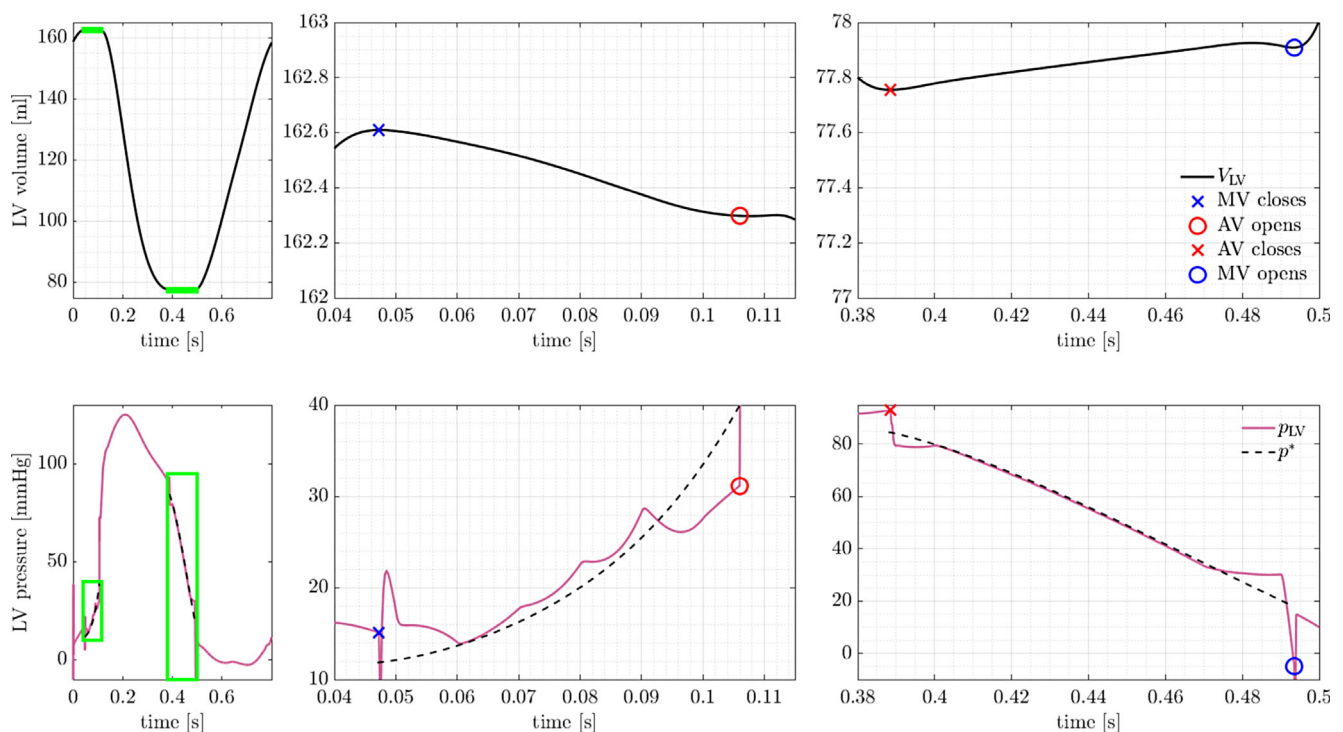


**FIGURE 16** Test C. Ventricular volume and pressures (obtained through the ARIIS method), with zoom on the isovolumetric phases.

augmented approach allows to simulate the isovolumetric phases, with a pressure evolution that is much more similar to the heart physiology.

In Figure 17, we show the pressure field (in mm Hg) on a clip in the LV apico-basal direction during the isovolumetric phases. The RIIS and ARIIS methods are characterized by different pressures, confirming our previous results. Moreover, we investigate the difference among the two solutions also in terms of velocity field, by showing a surface line integral convolution (LIC) representation on a slice in the LV apico-basal direction colored with velocity magnitude. Consistently with the findings of Reference 29, we notice that the augmented approach does not impact the velocity field and both solutions reproduce the same flow patterns. More quantitatively, we compute the velocity magnitude in a control volume in the LV. When the augmented formulation is active, we compute a maximum discrepancy between the RIIS and the ARIIS velocities equal to $2.21 \times 10^{-4}$ m/s, corresponding to a relative error (divided by the maximum RIIS velocity magnitude) equal to 0.29%.

## 3.4 | Test D: opening and closing the valves according to flow conditions

In this section, we show how the ARIIS method allows to simulate the whole heart cycle by opening and closing the valve in a way that is driven by the blood flow. Since the ventricular pressure is not well defined during isovolumetric phases, the standard RIIS method would enforce us to open and close the valve at prescribed times.[31] On the contrary, we instantaneously (i.e., in a single time step) open and close the valves according to the following rules[29,30]:

- a valve in closed configuration opens when the pressure jump across it becomes positive; we evaluate the pressure jump by averaging the pressure over spherical control volumes upstream and downstream of each valve (see Figure 18);
- a valve in open configuration closes when the flowrate through it changes sign; the flow rate is evaluated by computing the time derivative of the ventricular volume.
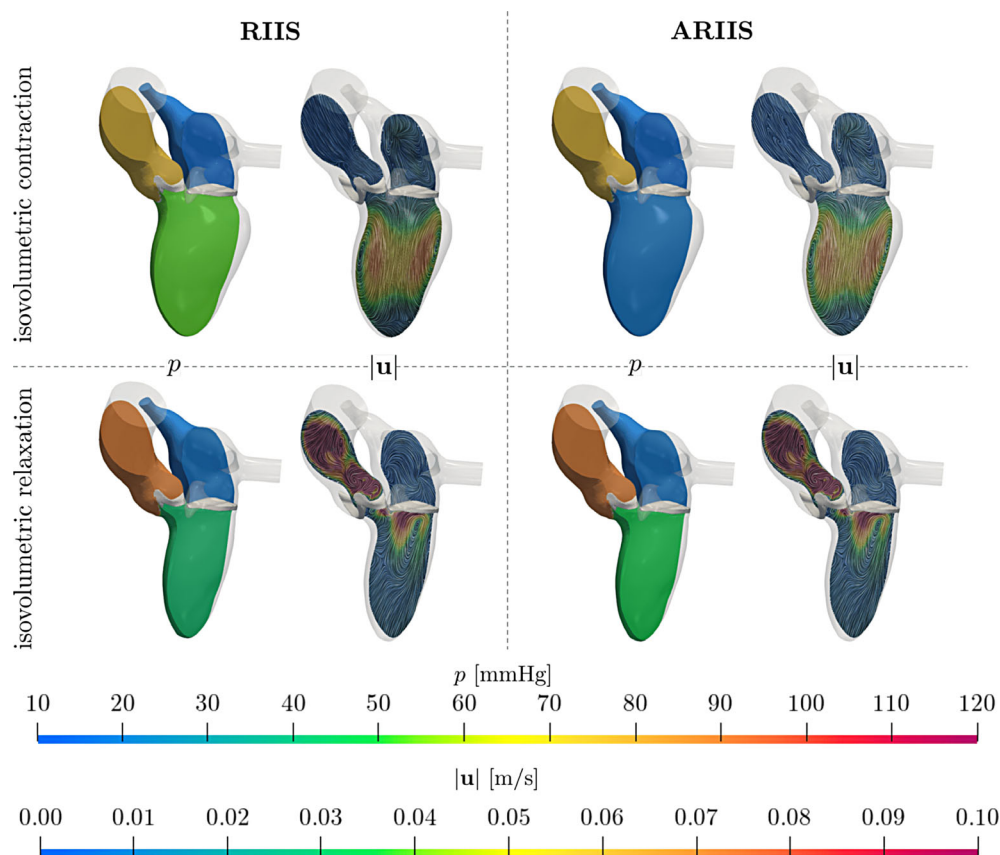


**FIGURE 17** Test C. Comparison between RIIS and ARIIS methods during isovolumetric phases: pressure on a clip in the LV apicobasal direction and a section colored according to velocity magnitude with a surface LIC representation.
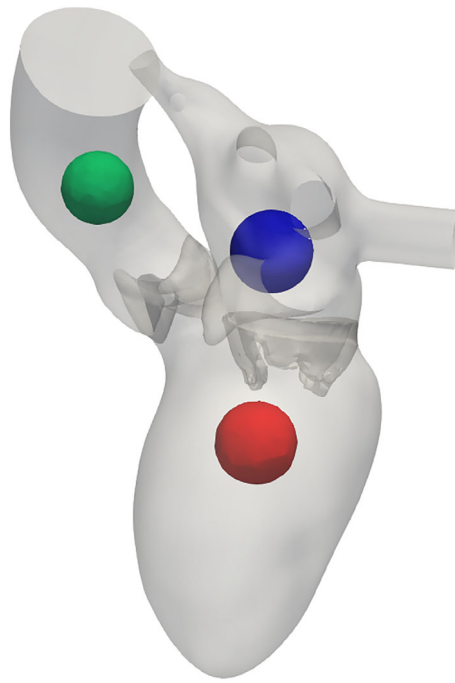
**FIGURE 18** Control volumes used to evaluate the average pressure jump across cardiac valves. A valve open when the pressure jump becomes positive.

We remark that this is a proof-of-concept test: a more physically sound model would result from combining the ARIIS method with more sophisticated valve displacement laws such as the models proposed in References 79,99. In the following, we consider both the case of the benchmark problem featuring ventricular contraction introduced in Test B (Section 3.2) and the cardiac case of Test C (Section 3.3).

### 3.4.1 | Benchmark problem including ventricular contraction

We carry out a simulation in the same setting of Section 3.2, except that the opening and closing times of valves are determined according to the aforementioned rules, rather than being prescribed. The results are reported in Figure 19. We obtain results that are consistent with those of Section 3.2, without the need to choose a priori the times at which valves open and close. As in Test B, very short oscillations can be observed due to the instantaneous closing of the valves, which however do not affect the overall flow and valve dynamics.

### 3.4.2 | Cardiac test case

We consider the cardiac test case introduced in Section 3.3 and we carry out the ARIIS simulation, opening and closing the valves according to blood flow conditions. We report the results of this simulation in Figure 20. Differently from RIIS, since the ARIIS method produces physiological ventricular pressure and close to the reference pressure $p^*$, we can successfully open both the mitral and the aortic valve when the downstream pressure reaches the upstream one.

## 4 | CONCLUSIONS, DISCUSSION AND LIMITATIONS

In this article, we proposed an augmented version of the Resistive Immersed Implicit Surface (RIIS) method[65] to correctly simulate the heart hemodynamics during isovolumetric phases. This Augmented RIIS (ARIIS) method extends the previously proposed Augmented Resistive Immersed Surface (ARIS) method[29] to the case of meshes that are non-conforming to cardiac valves.

**FIGURE 19**   Test D, cylinder benchmark, valves opening and closing according to flow conditions with the ARIIS method. Top: space-averaged pressures in control volumes in the three compartments of the cylinder. Middle: time derivative of the volume of the middle compartment. Bottom: computed (not prescribed) valve states versus time.
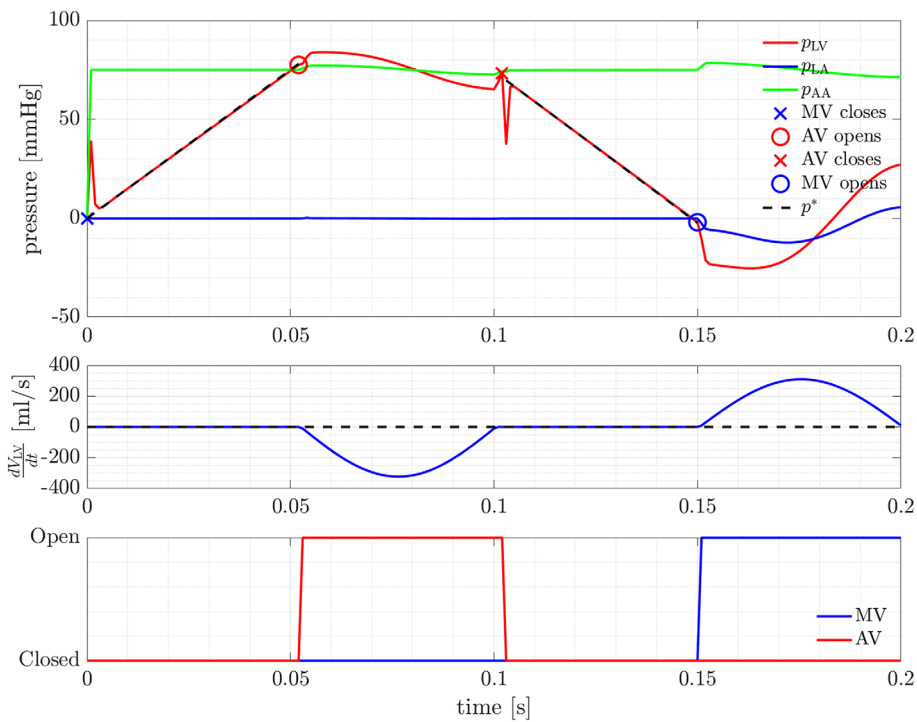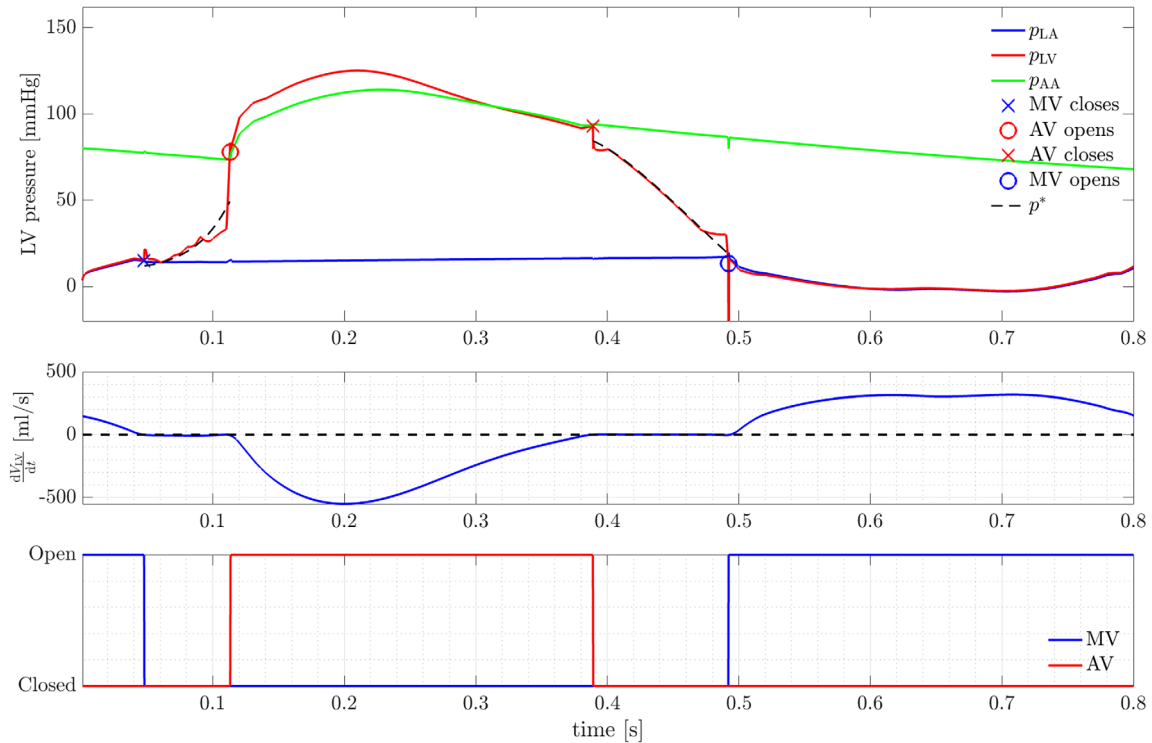


**FIGURE 20**   Test D, cardiac application: valves opening and closing according to flow conditions with the ARIIS method. Top: space-averaged pressures in control volumes located in LA, LV, AA (see Figure 18) and reference ventricular pressure versus time. Middle: time derivative of the LV volume. Bottom: computed (not prescribed) valve states versus time.

Starting from the RIIS method, and following analogous steps of the original ARIS method,[29] we derived the correction term required to simulate the intracardiac hemodynamics when both valves are closed. Specifically, as done in Reference 29, we introduced an additional term to the momentum balance of the Navier–Stokes equations that only acts on the valves and is only active during the isovolumetric phases. From the ARIIS derivation, and analogously with the original formulation of Reference 29, we found that the corrective term depends on the external pressure, the valve areas, the resistive term itself, and a prescribed (reference) pressure representing the intraventricular pressure transient when both valves are closed. The reference pressure can be imposed, for instance, from electromechanical simulations or from patient-specific data.

We applied the ARIIS method to three different problems: the same cylindrical toy problem introduced in 29 for the sake of validation of the proposed method, a novel benchmark problem retaining characteristics of a heart cycle, and the flow in a realistic human left heart geometry (with endocardium displacement obtained from electromechanical simulations).

All tests showed that the ARIIS method yields a ventricular pressure that closely follows the prescribed reference evolution. Moreover, we found that the accuracy of the results is not affected by resistance coefficient values. Since the ARIIS method produces physiological pressure transients during isovolumetric phases, we also showed that our method allows to open and close the valves in a way that is completely driven by the blood flow (i.e., according to pressure jump and reverse flow conditions). We believe this represents one of the main achievements of our work, since it avoids the need to prescribe opening and closing valve times.

The ARIIS method is very sensitive to small volume variations and oscillations during isovolumetric phases. Thus, further investigations are advisable for the employment of a better interpolant or approximant (in time) of the input displacement field. Moreover, we observed some mismatch between the fluid pressure and the electromechanical one, yielding an unphysical jump from the isovolumetric contraction to the ejection phase. This mismatch suggests a deeper investigation of the similarities and differences between electromechanics and CFD models, which will be the subject of future work. Additionally, a better reproduction of physiological data may be attained by relying on in-vivo pressure measurements in the definition of the reference pressure $p^*$: this represents an important direction of further investigation.

To conclude, the standard RIIS method yielded a ventricular pressure with large oscillations in time and inconsistent with physiology. Thus, these phases are often neglected in CFD cardiac simulations or, if included, valve opening and closing valve must be prescribed a priori. On the contrary, the perturbation term introduced by the proposed ARIIS method provided a valid approach to produce a far more physiological ventricular pressure. This allowed us to correctly simulate the isovolumetric phases, and hence to open and close the valves in a way that is completely driven by the blood flow, making the overall CFD model more physiologically sound. A further development in this direction will be the combination of the ARIIS method with more sophisticated valve displacement models based on the fluid stress exerted on the leaflets.[79,99]

## DATA AVAILABILITY STATEMENT

The data that support the findings of this study are available from the corresponding author upon reasonable request.

## ORCID

*Alberto Zingaro* https://orcid.org/0000-0002-1522-9647
*Michele Bucelli* https://orcid.org/0000-0003-3089-9734
*Ivan Fumagalli* https://orcid.org/0000-0001-9256-1398
*Luca Dede'* https://orcid.org/0000-0002-6558-8277

# ENDNOTES

\* https://lifex.gitlab.io/.

\*\* iHEART—An Integrated Heart model for the simulation of the cardiac function, European Research Council (ERC) grant agreement No. 740132, P.I. Prof. A. Quarteroni, 2017–2022.

† 528 computing nodes each $2 \times$ CPU Intel CascadeLake 8260, with 24 cores each, 2.4 GHz, 384 GB RAM. See https://wiki.u-gov.it/confluence/display/SCAIUS/UG3.3%3A+GALILEO100+UserGuide for technical specifications.

# REFERENCES

1. Quarteroni A, Dede′ L, Manzoni A, et al. *Mathematical Modelling of the Human Cardiovascular System: Data, Numerical Approximation, Clinical Applications*. Cambridge University Press; 2019.
2. Katz AM. *Physiology of the Heart*. Lippincott Williams & Wilkins; 2010.
3. Formaggia L, Lamponi D, Tuveri M, Veneziani A. Numerical modeling of 1D arterial networks coupled with a lumped parameters description of the heart. *Comput Methods Biomech Biomed Eng*. 2006;9(5):273-288.
4. Brenneisen J, Daub A, Gerach T, et al. Sequential coupling shows minor effects of fluid dynamics on myocardial deformation in a realistic whole-heart model. *Front Cardiovasc Med*. 2021;8(December):1-13.
5. Bucelli M, Dede′ L, Quarteroni A, Vergara C. Partitioned and monolithic FSI schemes for the numerical simulation of the heart. *Commun Comput Phys*. 2022;32:1217-1256.
6. Cheng Y, Oertel H, Schenkel T. Fluid-structure coupled CFD simulation of the left ventricular flow during filling phase. *Ann Biomed Eng*. 2005;33(5):567-576.
7. Khodaei S, Henstock A, Sadeghi R, et al. Personalized intervention cardiology with transcatheter aortic valve replacement made possible with a non-invasive monitoring and diagnostic framework. *Sci Rep*. 2021;11(1):1-28.
8. Nordsletten D, McCormick M, Kilner PJ, Hunter P, Kay D, Smith NP. Fluid–solid coupling for the investigation of diastolic and systolic human left ventricular function. *Int J Numer Methods Biomed Eng*. 2011;27(7):1017-1039.
9. Zhang Q, Hisada T. Analysis of fluid–structure interaction problems with structural buckling and large domain changes by ALE finite element method. *Comput Methods Appl Mech Eng*. 2001;190(48):6341-6357.
10. Bucelli M, Zingaro A, Africa PC, Fumagalli I, Dede′ L, Quarteroni AM. A mathematical model that integrates cardiac electrophysiology, mechanics and fluid dynamics: application to the human left heart. *Int J Numer Methods Biomed Eng*. 2022;39:e3678.
11. Santiago A, Aguado-Sierra J, Zavala-Aké M, et al. Fully coupled fluid-electro-mechanical model of the human heart for supercomputers. *Int J Numer Methods Biomed Eng*. 2018;34(12):e3140.
12. Watanabe H, Hisada T, Sugiura S, Okada J, Fukunari H. Computer simulation of blood flow, left ventricular wall motion and their interrelationship by fluid-structure interaction finite element method. *JSME Int J Ser C Mech Syst Mach Elem Manuf*. 2002;45(4):1003-1012.
13. Viola F, Meschini V, Verzicco R. Fluid–structure-electrophysiology interaction (FSE) in the leftheart: a multi-way coupled computational model. *Eur J Mech-B/Fluids*. 2020;79:212-232.
14. Choi YJ, Constantino J, Vedula V, Trayanova N, Mittal R. A new MRI-based model of heart function with coupled hemodynamics and application to normal and diseased canine left ventricles. *Front Bioeng Biotechnol*. 2015;3:140.
15. Tagliabue A, Dede′ L, Quarteroni A. Fluid dynamics of an idealized left ventricle: the extended Nitsche's method for the treatment of heart valves as mixed time varying boundary conditions. *Int J Numer Methods Fluids*. 2017;85(3):135-164.
16. Zingaro A, Dede′ L, Menghini F, Quarteroni A. Hemodynamics of the heart's left atrium based on a variational multiscale-LES numerical method. *Eur J Mech-B/Fluids*. 2021;89:380-400.
17. Domenichini F, Pedrizzetti G, Baccani B. Three-dimensional filling flow into a model left ventricle. *J Fluid Mech*. 2005;539:179-198.
18. Baccani B, Domenichini F, Pedrizzetti G. Vortex dynamics in a model left ventricle during filling. *Eur J Mech-B/Fluids*. 2002;21(5):527-543.
19. Mittal R, Seo Jung H, Vedula V, et al. Computational modeling of cardiac hemodynamics: current status and future outlook. *J Comput Phys*. 2016;305:1065-1082.
20. Corti M, Zingaro A, Dede′ L, Quarteroni A. Impact of atrial fibrillation on left atrium haemodynamics: a computational fluid dynamics study. *Comput Biol Med*. 2022;150:106143.
21. Fumagalli I, Fedele M, Vergara C, et al. An image-based computational hemodynamics study of the systolic anterior motion of the mitral valve. *Comput Biol Med*. 2020;123:103922.
22. This A, Morales Hernán G, Bonnefous O, Fernández Miguel A, Gerbeau J-F. A pipeline for image based intracardiac CFD modeling and application to the evaluation of the PISA method. *Comput Methods Appl Mech Eng*. 2020;358:112627.
23. Chnafa C, Mendez S, Nicoud F. Image-based large-eddy simulation in a realistic left heart. *Comput Fluids*. 2014;94:173-187.
24. Masci A, Alessandrini M, Forti D, et al. A proof of concept for computational fluid dynamic analysis of the left atrium in atrial fibrillation on a patient-specific basis. *J Biomech Eng*. 2020;142(1):011002.
25. Bennati L, Vergara C, Giambruno V, et al. An image-based computational fluid dynamics study of mitral regurgitation in presence of prolapse. *Cardiovasc Eng Technol*. 2023;14:457-475.
26. Bennati L, Giambruno V, Renzi F, et al. Turbulence and blood washout in presence of mitral regurgitation: a computational fluid-dynamics study in the complete left heart. *bioRxiv*; 2023;2023-03.

27. Karabelas E, Longobardi S, Fuchsberger J, et al. Global sensitivity analysis of four chamber heart hemodynamics using surrogate models. *IEEE Trans Biomed Eng*. 2022;69(10):3216-3223.

28. Augustin Christoph M, Crozier A, Neic A, et al. Patient-specific modeling of left ventricular electromechanics as a driver for haemodynamic analysis. *EP Europace*. 2016;18(suppl_4):iv121-iv129.

29. This A, Boilevin-Kayl L, Fernández Miguel A, Gerbeau J-F. Augmented resistive immersed surfaces valve model for the simulation of cardiac hemodynamics with isovolumetric phases. *Int J Numer Methods Biomed Eng*. 2020;36(3):e3223.

30. Zingaro A, Fumagalli I, Dede' L, et al. A geometric multiscale model for the numerical simulation of blood flow in the human left heart. *Discr Contin Dynam Syst S*. 2022;15(8):2391-2427.

31. Zingaro A, Bucelli M, Piersanti R, Regazzoni F, Dede' L, Quarteroni A. An electromechanics-driven fluid dynamics model for the simulation of the whole human heart. *arXiv Preprint arXiv:2301.02148*; 2023.

32. Zingaro A, Vergara C, Dede' L, Regazzoni F, Quarteroni A. A comprehensive mathematical model for cardiac perfusion. *arXiv Preprint arXiv:2303.13914*; 2023.

33. Fedele M, Piersanti R, Regazzoni F, et al. A comprehensive and biophysically detailed computational model of the whole human heart electromechanics. *Comput Methods Appl Mech Eng*. 2023;410:115983.

34. Cheng R, Lai Yong G, Chandran Krishnan B. Three-dimensional fluid-structure interaction simulation of bileaflet mechanical heart valve flow dynamics. *Ann Biomed Eng*. 2004;32(11):1471-1483.

35. Espino Daniel M, Shepherd Duncan ET, Hukins David WL. Evaluation of a transient, simultaneous, arbitrary Lagrange–Euler based multi-physics method for simulating the mitral heart valve. *Comput Methods Biomech Biomed Eng*. 2014;17(4):450-458.

36. Basting S, Quaini A, Čanić S, Glowinski R. Extended ALE method for fluid–structure interaction problems with large structural displacements. *J Comput Phys*. 2017;331:312-336.

37. Jianhai Z, Dapeng C, Shengquan Z. ALE finite element analysis of the opening and closing process of the artificial mechanical valve. *Appl Math Mech*. 1996;17(5):403-412.

38. Nestola Maria GC, Faggiano E, Vergara C, et al. Computational comparison of aortic root stresses in presence of stentless and stented aortic valve bio-prostheses. *Comput Methods Biomech Biomed Eng*. 2017;20(2):171-181.

39. Fernández Miguel A, Gerbeau J-F, Martin V. Numerical simulation of blood flows through a porous interface. *ESAIM: Math Modell Numer Anal*. 2008;42(6):961-990.

40. Astorino M, Hamers J, Shadden Shawn C, Gerbeau J-F. A robust and efficient valve model based on resistive immersed surfaces. *Int J Numer Methods Biomed Eng*. 2012;28(9):937-959.

41. Spühler Jeannette H, Jansson J, Jansson N, Hoffman J. 3D fluid-structure interaction simulation of aortic valves using a unified continuum ALE FEM model. *Front Physiol*. 2018;9:363.

42. Alauzet F, Fabrèges B, Fernández Miguel A, Landajuela M. Nitsche-XFEM for the coupling of an incompressible fluid with immersed thin-walled structures. *Comput Methods Appl Mech Eng*. 2016;301:300-335.

43. Hansbo P, Larson Mats G, Zahedi S. Characteristic cut finite element methods for convection–diffusion problems on time dependent surfaces. *Comput Methods Appl Mech Eng*. 2015;293:431-461.

44. Erik B, Fernández Miguel A. An unfitted Nitsche method for incompressible fluid–structure interaction using overlapping meshes. *Comput Methods Appl Mech Eng*. 2014;279:497-514.

45. Mayer Ursula M, Popp A, Gerstenberger A, WallWolfgang A. 3D fluid–structure–contact interaction based on a combined XFEM FSI and dual mortar contact approach. *Comput Mech*. 2010;46(1):53-67.

46. Massing A, Larson M, Logg A, Rognes M. A Nitsche-based cut finite element method for a fluid-structure interaction problem. *Commun Appl Math Comput Sci*. 2015;10(2):97-120.

47. Gerstenberger A, Wall Wolfgang A. An extended finite element method/Lagrange multiplier based approach for fluid–structure interaction. *Comput Methods Appl Mech Eng*. 2008;197(19–20):1699-1714.

48. Zonca S, Vergara C, Formaggia L. An unfitted formulation for the interaction of an incompressible fluid with a thick structure via an XFEM/DG approach. *SIAM J Sci Comput*. 2018;40(1):B59-B84.

49. Peskin CS. Flow patterns around heart valves: a numerical method. *J Comput Phys*. 1972;10(2):252-271.

50. Borazjani I, Ge L, Sotiropoulos F. High-resolution fluid–structure interaction simulations of flow through a bi-leaflet mechanical heart valve in an anatomic aorta. *Ann Biomed Eng*. 2010;38(2):326-344.

51. Griffith BE. Immersed boundary model of aortic heart valve dynamics with physiological driving and loading conditions. *Int J Numer Methods Biomed Eng*. 2012;28(3):317-345.

52. Hsu M-C, Kamensky D, Bazilevs Y, Sacks Michael S, Hughes Thomas JR. Fluid–structure interaction analysis of bioprosthetic heart valves: significance of arterial wall deformation. *Comput Mech*. 2014;54(4):1055-1071.

53. Wu Michael CH, Zakerzadeh R, Kamensky D, Kiendl J, Sacks Michael S, Hsu M-C. An anisotropic constitutive model for immersogeometric fluid–structure interaction analysis of bioprosthetic heart valves. *J Biomech*. 2018;74:23-31.

54. Liu Wing K, Liu Y, Farrell D, et al. Immersed finite element method and its applications to biological systems. *Comput Methods Appl Mech Eng*. 2006;195(13–16):1722-1749.

55. Yang J, Yu F, Krane M, Zhang LT. The perfectly matched layer absorbing boundary for fluid–structure interactions using the immersed finite element method. *J Fluids Struct*. 2018;76:135-152.

56. Nestola Maria GC, Becsek B, Zolfaghari H, et al. An immersed boundary method for fluid-structure interaction based on variational transfer. *J Comput Phys*. 2019;398:108884.

57. Oks D, Samaniego C, Houzeaux G, Butakoff C, Vázquez M. Fluid–structure interaction analysis of eccentricity and leaflet rigidity on thrombosis biomarkers in bioprosthetic aortic valve replacements. *Int J Numer Methods Biomed Eng*. 2022;38(12):e3649.

58. Glowinski R, Pan T-W, Periaux J. A Lagrange multiplier/fictitious domain method for the numerical simulation of incompressible viscous flow around moving rigid bodies: (I) case where the rigid body motions are known a priori. *C R l'Acad Sci-Ser I-Math*. 1997;324(3): 361-369.

59. Astorino M, Gerbeau J-F, Pantz O, Traore K-F. Fluid–structure interaction and multi-body contact: application to aortic valves. *Comput Methods Appl Mech Eng*. 2009;198(45–46):3603-3612.

60. Bazilevs Y, Hsu M-C, Kiendl J, Wüchner R, Bletzinger K-U. 3D simulation of wind turbine rotors at full scale. Part II: fluid–structure interaction modeling with composite blades. *Int J Numer Methods Fluids*. 2011;65(1–3):236-253.

61. Kamensky D, Hsu M-C, Schillinger D, et al. An immersogeometric variational framework for fluid–structure interaction: application to bioprosthetic heart valves. *Comput Methods Appl Mech Eng*. 2015;284:1005-1053.

62. De Hart J, Peters GWM, Schreurs PJG, Baaijens FPT. A three-dimensional computational analysis of fluid–structure interaction in the aortic valve. *J Biomech*. 2003;36(1):103-112.

63. Loon R, Anderson PD, Vosse FN. A fluid–structure interaction method with solid-rigid contact for heart valve dynamics. *J Comput Phys*. 2006;217(2):806-823.

64. Morsi Yos S, Yang William W, Wong Cynthia S, Das S. Transient fluid–structure coupling for simulation of a trileaflet heart valve using weak coupling. *J Artif Organs*. 2007;10(2):96-103.

65. Fedele M, Faggiano E, Dede' L, Quarteroni A. A patient-specific aortic valve model based on moving resistive immersed implicit surfaces. *Biomech Model Mechanobiol*. 2017;16(5):1779-1803.

66. Marom G. Numerical methods for fluid–structure interaction models of aortic valves. *Arch Comput Methods Eng*. 2015;22(4):595-620.

67. Votta E, Le TB, Stevanella M, et al. Toward patient-specific simulations of cardiac valves: state-ofthe-art and future directions. *J Biomech*. 2013;46(2):217-228.

68. Hirschhorn M, Tchantchaleishvili V, Stevens R, Rossano J, Throckmorton A. Fluid–structure interaction modeling in cardiovascular medicine – a systematic review 2017–2019. *Med Eng Phys*. 2020;78:1-13.

69. Schenkel T, Malve M, Reik M, Markl M, Jung B, Oertel H. MRI-based CFD analysis of flow in a human left ventricle: methodology and application to a healthy heart. *Ann Biomed Eng*. 2009;37(3):503-515.

70. Bavo AM, Pouch Alison M, Degroote J, et al. Patient-specific CFD models for intraventricular flow analysis from 3D ultrasound imaging: comparison of three clinical cases. *J Biomech*. 2017;50:144-150.

71. Quarteroni A, Sacco R, Saleri F. *Numerical Mathematics*. Springer Science & Business Media; 2010.

72. Doyle MG, Tavoularis S, Bougault Y. Application of fluid-structure interaction to numerical simulations in the left ventricle. *Trans Can Soc Mech Eng*. 2015;39(4):749-766.

73. Küttler U, Förster C, Wall WA. A solution for the incompressibility dilemma in partitioned fluid–structure interaction with pure Dirichlet fluid domains. *Comput Mech*. 2006;38:417-429.

74. Perktold K, Thurner E, Kenner T. Flow and stress characteristics in rigid walled and compliant carotid artery bifurcation models. *Med Biol Eng Comput*. 1994;32(1):19-26.

75. Taylor CA, Hughes TJR, Zarins CK. Finite element modeling of blood flow in arteries. *Comput Methods Appl Mech Eng*. 1998;158(1–2): 155-196.

76. Formaggia L, Quarteroni A, Veneziani A. *Cardiovascular Mathematics: Modeling and Simulation of the Circulatory System*. Springer Science & Business Media; 2010.

77. Donea J, Giuliani S, Halleux J-P. An arbitrary Lagrangian-Eulerian finite element method for transient dynamic fluid-structure interactions. *Comput Methods Appl Mech Eng*. 1982;33(1–3):689-723.

78. Hughes TJR, Liu WK, Zimmermann TK. Lagrangian-Eulerian finite element formulation for incompressible viscous flows. *Comput Methods Appl Mech Eng*. 1981;29(3):329-349.

79. Fumagalli I. A reduced 3D-0D FSI model of the aortic valve including leaflets curvature. *arXiv Preprint arXiv:2106.00571*; 2021.

80. Quarteroni A. *Numerical Models for Differential Problems*. Springer; 2017.

81. Tezduyar TE. Stabilized finite element formulations for incompressible flow computations. In: Hutchinson John W, Wu Theodore Y, eds. *Advances in Applied Mechanics*. Elsevier; 1991:1-44.

82. Bazilevs Y, Calo VM, Cottrell JA, Hughes Thomas JR, Reali A, Scovazzi G. Variational multiscale residual-based turbulence modeling for large eddy simulation of incompressible flows. *Comput Methods Appl Mech Eng*. 2007;197(1–4):173-201.

83. Forti D, Dede' L. Semi-implicit BDF time discretization of the Navier–stokes equations with VMS-LES modeling in a high performance computing framework. *Comput Fluids*. 2015;117:168-182.

84. Jasak H, Tukovic Z. Automatic mesh motion for the unstructured finite volume method. *Transa FAMENA*. 2006;30(2):1-20.

85. Africa PC. lifex: a flexible, high performance library for the numerical solution of complex finite elements. *SoftwareX*. 2022;20:101252.

86. Africa PC, Piersanti R, Fedele M, Dede' L, Quarteroni A. Lifex-fiber: an open tool for myofibers generation in cardiac computational models. *BMC Bioinform*. 2023;24(1):143.

87. Arndt D, Bangerth W, Blais B, et al. The deal.II library, version 9.3. *J Numer Math*. 2021;29:29-186.

88. Arndt D, Bangerth W, Davydov D, et al. The deal.II finite element library: design, features, and insights. *Comput Math Appl*. 2020;81: 407-422.

89. Official deal.ii website. https://www.dealii.org/

90. Africa PC, Fumagalli I, Bucelli M, et al. lifex-cfd: an open-source computational fluid dynamics solver for cardiovascular applications. arXiv preprint arXiv:2304.12032 2023.

91. Africa PC, Fumagalli I, Bucelli M, et al. Lifex-cfd: an open-source computational fluid dynamics solver for cardiovascular applications. *arXiv Preprint arXiv:2304.12032*; 2023. doi:10.5281/zenodo.7852089

92. Blanco Pablo J, Feijoo Raul A. A 3D-1D-0D computational model for the entire cardiovascular system. *Mecan Comput*. 2010;24:5887-5911.

93. Hirschvogel M, Bassilious M, Jagschies L, Wildhirt SM, Gee MW. A monolithic 3D-0D coupled closed-loop model of the heart and the vascular system: experiment-based parameter estimation for patient-specific cardiac mechanics. *Int J Numer Methods Biomed Eng*. 2017;33(8):e2842.

94. Regazzoni F, Salvador M, Africa PC, Fedele M, Dede′ L, Quarteroni A. A cardiac electromechanical model coupled with a lumped-parameter model for closed-loop blood circulation. *J Comput Phys*. 2022;457:111083.

95. Inc Zygote Media Group. Zygote solid 3D heart generation II development report. *Technical Development of 3D Anatomical Systems*; 2014.

96. Antiga L, Piccinelli M, Botti L, Ene-Iordache B, Remuzzi A, Steinman DA. An imagebased modeling framework for patient-specific computational hemodynamics. *Med Biol Eng Comput*. 2008;46(11):1097-1112.

97. Fedele M, Quarteroni AM. Polygonal surface processing and mesh generation tools for numerical simulations of the complete cardiac function. *Int J Numer Methods Biomed Eng*. 2021;37:e3435.

98. De Boor C. *A Practical Guide to Splines*. Springer-Verlag; 1978.

99. Korakianitis T, Shi Y. Numerical simulation of cardiovascular dynamics with healthy and diseased heart valves. *J Biomech*. 2006; 39(11):1964-1982.

100. Ten Tusscher Kirsten HWJ, Panfilov AV. Alternans and spiral breakup in a human ventricular tissue model. *Am J Physiol Heart Circ Physiol*. 2006;291(3):H1088-H1100.

101. Colli FP, Pavarino LF, Scacchi S. *Mathematical Cardiac Electrophysiology*. Springer; 2014.

102. Salvador M, Regazzoni F, Pagani S, et al. The role of mechano-electric feedbacks and hemodynamic coupling in scar-related ventricular tachycardia. *Comput Biol Med*. 2022;142:105203.

103. Regazzoni F, Dede′ L, Quarteroni A. Biophysically detailed mathematical models of multiscale cardiac active mechanics. *PLoS Comput Biol*. 2020;16(10):e1008294.

104. Usyk TP, Mazhari R, McCulloch AD. Effect of laminar orthotropic myofiber architecture on regional stress and strain in the canine left ventricle. *J Elast Phys Sci Solids*. 2000;61(1):143-164.

**How to cite this article:** Zingaro A, Bucelli M, Fumagalli I, Dede′ L, Quarteroni A. Modeling isovolumetric phases in cardiac flows by an Augmented Resistive Immersed Implicit Surface method. *Int J Numer Meth Biomed Engng*. 2023;39(12):e3767. doi:10.1002/cnm.3767

# APPENDIX A

## A.1 | THE ELECTROMECHANICAL MODEL

In this section, we briefly describe the electromechanical model used to provide the boundary displacement in Section 3.3. We refer to Reference 94 for additional details on the models and on the methods used for their solution. Let $\widehat{\Omega}$ be the domain occupied by the ventricular walls, in reference (undeformed and stress-free) configuration. The unknowns of the model are the following variables:

$$v : \widehat{\Omega} \times (0, T) \to \mathbb{R} \qquad \text{transmembrane potential,}$$

$$\mathbf{w} : \widehat{\Omega} \times (0, T) \to \mathbb{R}^{N_{\mathrm{ion}}} \qquad \text{ionic state variables,}$$

$$\mathbf{s} : \widehat{\Omega} \times (0, T) \to \mathbb{R}^{N_{\mathrm{act}}} \qquad \text{activation state variables,}$$

$$\mathbf{d} : \widehat{\Omega} \times (0, T) \to \mathbb{R}^{3} \qquad \text{solid displacement,}$$

$$\mathbf{c} : (0, T) \to \mathbb{R}^{N_{\mathrm{circ}}} \qquad \text{circulation state variables.}$$

The evolution of the ionic variables is regulated by the model by 10 Tusscher and Panfilov,[100] which can be expressed as the following system of ODEs:

$$
\begin{cases}
\dfrac{\partial \mathbf{w}}{\partial t} = \mathbf{F}_{\text{ion}}(\mathbf{w}, v) & \text{in } \widehat{\Omega} \times (0, T), \\
\mathbf{w} = \mathbf{w}_0 & \text{in } \widehat{\Omega} \times \{0\}.
\end{cases}
$$

We refer to Reference 100 for the definition of $\mathbf{F}_{\text{ion}}(\mathbf{w}, v)$. One of the entries of $\mathbf{w}$ is the intracellular calcium concentration, denoted by $\left[\text{Ca}^{2+}\right]_{\text{i}}$. The evolution of the transmembrane potential is described by the monodomain equation with mechano-electrical feedbacks[101,102]:

$$
\begin{cases}
Jvt - \boldsymbol{\nabla} \cdot \left(JF^{-1}D_m F^{-T}\boldsymbol{\nabla}v\right) + JI_{\text{ion}}(v, \mathbf{w}) = JI_{\text{app}} & \text{in } \widehat{\Omega} \times (0, T), \\
JF^{-1}D_m F^{-T}\boldsymbol{\nabla}v \cdot \mathbf{n} = 0 & \text{on } \partial\widehat{\Omega} \times (0, T), \\
v = v_0 & \text{in } \widehat{\Omega} \times \{0\}.
\end{cases}
\tag{A1}
$$

In the above, $F = I + \boldsymbol{\nabla}\mathbf{d}$, $J = \det F$, and $D_m$ is a conductivity tensor, defined as

$$
D_m = \sigma_m^{\text{l}} \frac{F\mathbf{f}_0 \otimes F\mathbf{f}_0}{\|F\mathbf{f}_0\|^2} + \sigma_m^{t} \frac{F\mathbf{s}_0 \otimes F\mathbf{s}_0}{\|F\mathbf{s}_0\|^2} + \sigma_m^{n} \frac{F\mathbf{n}_0 \otimes F\mathbf{n}_0}{\|F\mathbf{n}_0\|^2},
$$

where, $\{\mathbf{f}_0, \mathbf{s}_0, \mathbf{n}_0\}$ is an orthonormal triplet that, at every point in $\widehat{\Omega}$, describes the local orientation of muscular fibers, sheets of fibers and fiber normal direction. In (A1), $I_{\text{app}}$ is an applied current providing the initial stimulus, and $I_{\text{ion}}$ is defined by the ionic model.[100]

The state of contraction, described by the vector $\mathbf{s}$, evolves according to the RDQ20-MF model,[103] which can be expressed as a system of ODEs:

$$
\begin{cases}
\dfrac{\partial \mathbf{s}}{\partial t} = \mathbf{F}_{\text{act}}\left(\mathbf{s}, \left[\text{Ca}^{2+}\right]_{\text{i}}, \mathbf{d}, \mathbf{d}t\right) & \text{in } \widehat{\Omega} \times (0, T), \\
\mathbf{s} = \mathbf{s}_0 & \text{in } \widehat{\Omega} \times \{0\}.
\end{cases}
$$

The model defines an active stress tensor as

$$
P_{\text{act}}(\mathbf{d}, \mathbf{s}) = T_{\text{act}}(\mathbf{s}) \frac{F\mathbf{f}_0 \otimes \mathbf{f}_0}{\|F\mathbf{f}_0\|}.
$$

We refer to Reference 103 for the definition of the functions $\mathbf{F}_{\text{act}}$ and $T_{\text{act}}$.

The evolution of the displacement $\mathbf{d}$ is regulated by the elastodynamics equation

$$
\begin{cases}
\rho_s \dfrac{\partial^2 \mathbf{d}}{\partial t^2} - \boldsymbol{\nabla} \cdot P(\mathbf{d}, \mathbf{s}) = \mathbf{0} & \text{in } \widehat{\Omega} \times (0, T), \\
\mathbf{d} = \mathbf{0} & \text{on } \widehat{\Gamma}^{\text{base}} \times (0, T), \\
P(\mathbf{d}, \mathbf{s})\mathbf{n} = -(\mathbf{n} \otimes \mathbf{n})\left(K_\perp^{\text{epi}}\mathbf{d} + C_\perp^{\text{epi}}\mathbf{d}t\right) - (I - \mathbf{n} \otimes \mathbf{n})\left(K_\parallel^{\text{epi}}\mathbf{d} + C_\parallel^{\text{epi}}\mathbf{d}t\right) & \text{on } \widehat{\Gamma}^{\text{epi}} \times (0, T), \\
P(\mathbf{d}, \mathbf{s})\mathbf{n} = -JF^{-T}p_{\text{LV}} & \text{on } \widehat{\Gamma}^{\text{endo}} \times (0, T), \\
\widehat{\mathbf{d}} = \widehat{\mathbf{d}}_0 & \text{in } \widehat{\Omega} \times \{0\}, \\
\dfrac{\partial \mathbf{d}}{\partial t} = \mathbf{0} & \text{in } \widehat{\Omega} \times \{0\}.
\end{cases}
\tag{A2}
$$

In the above, $\rho_s$ is the solid density, and $P(\mathbf{d}, \mathbf{s})$ is the stress tensor, defined as

$$P(\mathbf{d}, \mathbf{s}) = P_{\text{pas}}(\mathbf{d}) + P_{\text{act}}(\mathbf{d}, \mathbf{s}).$$

The passive contribution $P_{\text{pas}}(\mathbf{d})$ is defined according to the Guccione constitutive law, as reported in Reference 104. $\widehat{\Gamma}^{\text{base}}$, $\widehat{\Gamma}^{\text{epi}}$ and $\widehat{\Gamma}^{\text{endo}}$ are the portions of $\partial\widehat{\Omega}$ corresponding to the ventricular base, epicardium and endocardium respectively. The coefficients $K_{\perp}^{\text{epi}}$, $K_{\parallel}^{\text{epi}}$, $C_{\perp}^{\text{epi}}$ and $C_{\parallel}^{\text{epi}}$ account for the interaction of the ventricle with the pericardial sac and the surrounding organs. The pressure $p_{\text{LV}}$ is one of the entries of the circulation state vector $\mathbf{c}$.

The evolution of the latter is described by a system of ODEs whose unknowns are pressures and blood flows in several compartments of the circulatory system:

$$\begin{cases} \dfrac{\partial \mathbf{c}}{\partial t} = \mathbf{F}_{\text{circ}}(\mathbf{c}, t) & \text{in } (0, T), \\ \mathbf{c}(0) = \mathbf{c}_0. \end{cases}$$

We refer to Reference 94 for the definition of $\mathbf{F}_{\text{circ}}$. The circulation model is bidirectionally coupled to the mechanics equations (A2), through the boundary condition on $\widehat{\Gamma}^{\text{endo}}$ and by imposing that the volume of the ventricular chamber as computed by the circulation model is the same as that obtained in the mechanics model.

The coupled electromechanical model is solved by means of the segregated-intergrid-staggered scheme introduced in Reference 94. After the simulation, the endocardial displacement $\mathbf{d}|_{\widehat{\Gamma}^{\text{endo}}}$ is extracted, extended to zero on the boundaries of atrium and ascending aorta, and used as input for the CFD simulation of Test C (Section 3.3).

The values of the parameters of the monodomain, force generation and mechanics models are reported in Table A1, whereas Tables A2 and A3 report those for the circulation model. The values of parameters for the ionic model are the same as in the original paper.[100]

**TABLE A1** Parameters used in the electromechanical model: electrophysiology (EP), active force generation (AFG), and solid mechanics (M).

| Physics | Parameter | Value | | |
|---------|-----------|-------|---|---|
| EP | Conductivities | $\sigma_m^l$ | $2.00 \times 10^{-4}$ | $\text{m}^2/\text{s}$ |
| | | $\sigma_m^t$ | $1.05 \times 10^{-4}$ | $\text{m}^2/\text{s}$ |
| | | $\sigma_m^n$ | $0.55 \times 10^{-4}$ | $\text{m}^2/\text{s}$ |
| | Stimulus | $A_{\text{app}}$ | 25.71 | V/s |
| | | $\sigma_{\text{app}}$ | $5 \times 10^{-3}$ | m |
| | | $T_{\text{app}}$ | $3 \times 10^{-3}$ | s |
| AFG | | $\gamma$ | 30 | |
| | | $k_d$ | 0.36 | |
| | | $\alpha_{k_d}$ | $-0.2083$ | |
| | | $K_{\text{off}}$ | 8 | 1/s |
| | | $K_{\text{basic}}$ | 4 | 1/s |
| | | $\mu_{fp}^0$ | 32.255 | 1/s |
| | | $\mu_{fp}^1$ | 0.768 | 1/s |
| | | $a_{\text{XB}}$ | $20 \times 10^8$ | Pa |

(Continues)

**TABLE A1** (Continued)

| Physics | Parameter | Value | | |
|---|---|---|---|---|
| M | Guccione | $\rho_s$ | 1000 | kg/m$^2$ |
| | | $c$ | $8.8 \times 10^2$ | Pa |
| | | $a_{\text{ff}}$ | 8 | |
| | | $a_{\text{ss}}$ | 6 | |
| | | $a_{\text{nn}}$ | 3 | |
| | | $a_{\text{fs}}$ | 12 | |
| | | $a_{\text{fn}}$ | 3 | |
| | | $a_{\text{sn}}$ | 3 | |
| | | $\kappa$ | $5 \times 10^4$ | Pa |
| | | $K_\perp^{\text{epi}}$ | $2 \times 10^5$ | Pa/m |
| | Boundary conditions | $K_\parallel^{\text{epi}}$ | $2 \times 10^4$ | Pa/m |
| | | $C_\perp^{\text{epi}}$ | $2 \times 10^4$ | Pa s/m |
| | | $C_\parallel^{\text{epi}}$ | $2 \times 10^3$ | Pa s/m |
| | In. conditions | $p_0$ | 1333.2 | Pa |

*Note*: For the force generation model, we only report parameters that are different from the original setting described in Reference [103].

**TABLE A2** Parameters of the circulation model for the ventricular electromechanical simulation: external circulation.

| | Parameter | Value | |
|---|---|---|---|
| Systemic arteries | $R_{\text{AR}}^{\text{SYS}}$ | 0.3750 | mm Hg s/mL |
| | $C_{\text{AR}}^{\text{SYS}}$ | 2.048 | mm/mm Hg |
| | $L_{\text{AR}}^{\text{SYS}}$ | 2.7e−3 | mm Hg s$^2$/mL |
| | $R_{\text{upstream}}^{\text{SYS}}$ | 0.05 | mm Hg s/mL |
| | $p_{\text{AR}}^{\text{SYS}}(0)$ | 80.0 | Pa |
| | $Q_{\text{AR}}^{\text{SYS}}(0)$ | 0.0 | mL/s |
| Systemic veins | $R_{\text{VEN}}^{\text{SYS}}$ | 0.26 | mm Hg s/mL |
| | $C_{\text{VEN}}^{\text{SYS}}$ | 60.0 | mL/mm Hg |
| | $L_{\text{VEN}}^{\text{SYS}}$ | 5e−4 | mm Hg s$^2$/mL |
| | $p_{\text{VEN}}^{\text{SYS}}(0)$ | 30.9 | Pa |
| | $Q_{\text{VEN}}^{\text{SYS}}(0)$ | 0.0 | |
| Pulmonary arteries | $R_{\text{AR}}^{\text{PUL}}$ | 0.05 | mm Hg s/mL |
| | $C_{\text{AR}}^{\text{PUL}}$ | 10.0 | mL/mm Hg |
| | $L_{\text{AR}}^{\text{PUL}}$ | 5e−4 | mm Hg s$^2$/mL |
| | $p_{\text{AR}}^{\text{PUL}}(0)$ | 29.34 | Pa |
| | $Q_{\text{AR}}^{\text{PUL}}(0)$ | 0.0 | mL/s |
| Pulmonary veins | $R_{\text{VEN}}^{\text{PUL}}$ | 0.025 | mm Hg s/mL |
| | $C_{\text{VEN}}^{\text{PUL}}$ | 38.4 | mL/mm Hg |
| | $L_{\text{VEN}}^{\text{PUL}}$ | 2.083e−4 | mm Hg s$^2$/mL |
| | $p_{\text{VEN}}^{\text{PUL}}(0)$ | 13.58 | Pa |
| | $Q_{\text{VEN}}^{\text{PUL}}(0)$ | 0.0 | mL/s |

*Note*: The same parameters are employed for the 3D-0D CFD simulation.

**TABLE A3**  Parameters of the circulation model for the ventricular electromechanical simulation: cardiac circulation.

|  | Parameter | Value |  |
|---|---|---|---|
| Left atrium | $E_A$ | 0.07 | mm Hg/mL |
|  | $E_B$ | 0.09 | mm Hg/mL |
|  | $t_C$ | 0.80 |  |
|  | $T_C$ | 0.17 |  |
|  | $T_R$ | 0.17 |  |
|  | $V_{LA}(0)$ | 79.5 | mL |
| Right atrium | $E_A$ | 0.06 | mm Hg/mL |
|  | $E_B$ | 0.07 | mm Hg/mL |
|  | $t_C$ | 0.80 |  |
|  | $T_C$ | 0.17 |  |
|  | $T_R$ | 0.17 |  |
|  | $V_{LA}(0)$ | 64.17 | mL |
| Right ventricle | $E_A$ | 0.55 | mm Hg/mL |
|  | $E_B$ | 0.05 | mm Hg/mL |
|  | $t_C$ | 0.0 |  |
|  | $T_C$ | 0.34 |  |
|  | $T_R$ | 0.15 |  |
|  | $V_{LA}(0)$ | 148.9 | mL |
| Mitral valve | $R_{min}$ | 0.0164 | mm Hg s/mL |
|  | $R_{max}$ | 75,006.2 | mm Hg s/mL |
| Aortic valve | $R_{min}$ | 0.0355 | mm Hg s/mL |
|  | $R_{max}$ | 75,006.2 | mm Hg s/mL |
| Tricuspid valve | $R_{min}$ | 0.0075 | mm Hg s/mL |
|  | $R_{max}$ | 75,006.2 | mm Hg s/mL |
| Pulmonary valve | $R_{min}$ | 0.0075 | mm Hg s/mL |
|  | $R_{max}$ | 75,006.2 | mm Hg s/mL |

*Note*: Initial time of contraction $t_c$, contraction duration $T_C$ and relaxation duration $T_R$ are relative to the heartbeat period. For the right atrium, right ventricle, tricuspid and pulmonary valves, the same parameters are employed for the 3D-0D CFD simulation.